

คอมโพสิตของ LiBH_4 และ MgH_2 ที่บดก่อนซึ่งบรรจุระดับนาโนใน
วัสดุคาร์บอนแอโรเจลสแกฟโฟลด์สำหรับเป็นแหล่งกักเก็บไฮโดรเจน
แบบผันกลับได้



วิทยานิพนธ์นี้เป็นส่วนหนึ่งของการศึกษาตามหลักสูตรปริญญาวิทยาศาสตรมหาบัณฑิต
สาขาวิชาเคมี
มหาวิทยาลัยเทคโนโลยีสุรนารี
ปีการศึกษา 2556

**COMPOSITE OF LiBH_4 -PREMILLED MgH_2
NANOCONFINED IN CARBON AEROGEL SCAFFOLD
FOR REVERSIBLE HYDROGEN STORAGE**



**A Thesis Submitted in Partial Fulfillment of the Requirements for the
Degree of Master of Science in Chemistry
Suranaree University of Technology
Academic Year 2013**

**COMPOSITE OF LiBH₄-PREMILLED MgH₂ NANOCONFINED
IN CARBON AEROGEL SCAFFOLD FOR REVERSIBLE
HYDROGEN STORAGE**

Suranaree University of Technology has approved this thesis submitted in partial fulfillment of the requirements for a Master's Degree.

Thesis Examining Committee

(Assoc. Prof. Dr. Jatuporn Wittayakun)

Chairperson

(Asst. Prof. Dr. Rapee Gosalawit-Utke)

Member (Thesis Advisor)

(Asst. Prof. Dr. Sanchai Prayoonpokarach)

Member

(Asst. Prof. Dr. Kunwadee Rangriwatananon)

Member

(Prof. Dr. Sukit Limpijumnong)

Vice Rector for Academic Affairs
and Innovation

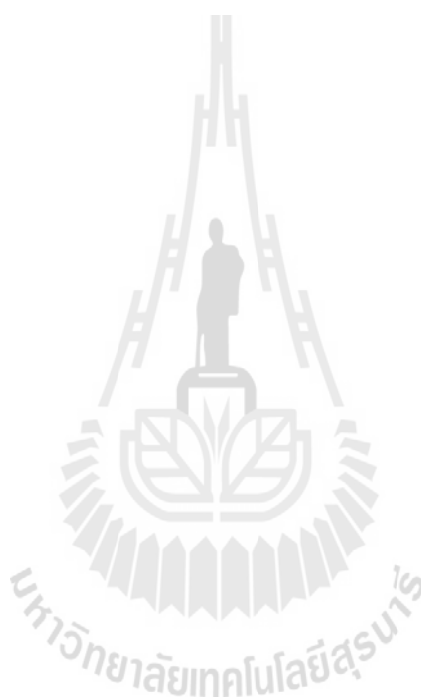
(Assoc. Prof. Dr. Prapun Manyum)

Dean of Institute of Science

โศภิตา เทียงวิริยะ : คอมโพสิตของ LiBH_4 และ MgH_2 ที่บดก่อนซึ่งบรรจุระดับนาโนในวัสดุคาร์บอนแอโรเจลสแคฟโฟลด์สำหรับเป็นแหล่งกักเก็บไฮโดรเจนแบบผันกลับได้ (COMPOSITE OF LiBH_4 -PREMILLED MgH_2 NANOCONFINED IN CARBON AEROGEL SCAFFOLD FOR REVERSIBLE HYDROGEN STORAGE)
อาจารย์ที่ปรึกษา : ผู้ช่วยศาสตราจารย์ ดร.ระพี โกศลวิตร-อุทเคอ, 84 หน้า.

โลหะเบาของสารจำพวกไฮไดรด์ได้รับความนิยมมากสำหรับการประยุกต์ใช้ในการกักเก็บไฮโดรเจนแบบของแข็ง (solid state hydride) แต่อย่างไรก็ตามก็ยังมีข้อเสียอยู่คือ การปล่อยและการกักเก็บไฮโดรเจนยังเกิดปฏิกิริยาช้าและใช้อุณหภูมิสูงอยู่ ดังนั้นเพื่อที่จะแก้ไขปัญหานี้ เราจะใช้ทฤษฎี reactive hydride composite (RHC) ซึ่งในตัวอย่างไฮไดรด์ทั้งหมด ลิเทียมโบโรไฮไดรด์ (LiBH_4) มีคุณสมบัติที่เหมาะสมที่สุด ดังนั้นเราจึงเลือกลิเทียมโบโรไฮไดรด์มาผสมรวมกับแมกนีเซียมไฮไดรด์ (MgH_2) ซึ่งระบบนี้จะช่วยเพิ่มความเร็วของการคายและการกักเก็บไฮโดรเจนได้ดียิ่งขึ้น เนื่องจากระหว่างการเกิดปฏิกิริยาคายไฮโดรเจนจะเกิดสารประกอบแมกนีเซียมโบไรด์ (MgB_2) ขึ้น นอกจากนี้พลังงานที่ใช้ในการคายและการกักเก็บไฮโดรเจนยังลดลงกว่าระบบที่เป็นลิเทียมโบโรไฮไดรด์ตัวเดียว ซึ่งปฏิกิริยาเกิดขึ้นดังสมการ $2\text{LiBH}_4 + \text{MgH}_2 \leftrightarrow \text{LiH} + \text{MgB}_2 + 4\text{H}_2$ แต่อย่างไรก็ตามแม้ว่าพลังงานที่ใช้จะลดลงแล้วแต่อุณหภูมิที่เกิดปฏิกิริยายังสูงอยู่ ดังนั้นเพื่อที่จะแก้ไขข้อเสียนี้ได้ นำสารผสมนี้มาทำการบรรจุระดับนาโนเมตร (nanoconfinement) ด้วยวิธีการหลอมเหลวสารให้เข้าไปอยู่ในรูพรุนของคาร์บอนแอโรเจลสแคฟโฟลด์ (carbon aerogel scaffold, CAS) เนื่องจากมันมีข้อดีคือ จะช่วยเพิ่มพื้นที่ผิวให้การเกิดปฏิกิริยา ทำให้สารมีโอกาสสัมผัสกันและเกิดปฏิกิริยาได้เร็วขึ้น แต่ระบบนี้ก็ยังมีข้อเสียคือต้องการความดันและอุณหภูมิสูงในการคายและกักเก็บไฮโดรเจน ดังนั้นในงานนี้เราได้ศึกษาสารประกอบระหว่าง 2LiBH_4 และ MgH_2 โดยการหลอมเหลวสารนี้เข้าไปในรูพรุนของคาร์บอน นอกจากนี้ก่อนที่จะหลอมเหลวสารเราได้บด MgH_2 ก่อนเพื่อลดขนาดอนุภาคของสารลงซึ่งจะทำให้การบรรจุนี้ดีขึ้น โดยลดอัตราส่วนโดยน้ำหนักของคาร์บอนต่อสารไฮไดรด์ลงจากงานที่แล้วเดิมใช้อัตราส่วน 2:1 เป็น 1:1 เพื่อที่จะเพิ่มความจุในการกักเก็บไฮโดรเจน และเพื่อยืนยันว่าสารนี้ได้บรรจุเข้าไปในรูพรุนของคาร์บอนแล้วเราสามารถยืนยันได้ด้วยเทคนิค N_2 adsorption-desorption และ SEM-EDS-mapping สำหรับตัวอย่างที่บรรจุระดับนาโนเมตรของ LiBH_4 และ บด MgH_2 ก่อน เมื่อเกิดการคายไฮโดรเจนจะเกิดเพียงแค่ขั้นตอนเดียวที่อุณหภูมิ 345 องศาเซลเซียส และไม่คายก๊าซไดโบเรน (B_2H_6) ออกมา แต่สารตัวอย่างที่ไม่บด MgH_2 ก่อนจะเกิดการคายไฮโดรเจนหลายขั้นตอนและคายก๊าซไดโบเรนออกมาด้วยระหว่างเกิดปฏิกิริยา และเกิดที่อุณหภูมิสูง (มากกว่า 430 องศาเซลเซียส) นอกจากนี้ยังลด

พลังงานกระตุ้นในการเกิดปฏิกิริยาลดถึง 16.8-138 kJ/mol เมื่อเทียบกับตัวอย่างที่ไม่ได้บด MgH_2 ก่อน และตัวอย่างที่บด MgH_2 ก่อนยังทำให้การเกิดปฏิกิริยาการคายไฮโดรเจนเกิดขึ้นที่อุณหภูมิต่ำที่ 320 องศาเซลเซียส เมื่อเทียบกับวิธีอื่นๆที่ใช้พัฒนาระบบของ $2LiBH_4-MgH_2$



สาขาวิชาเคมี
ปีการศึกษา 2556

ลายมือชื่อนักศึกษา _____
ลายมือชื่ออาจารย์ที่ปรึกษา _____

SOPHIDA TIANGWIRIYA : COMPOSITE OF LiBH₄-PREMILLED MgH₂
NANOCONFINED IN CARBON AEROGEL SCAFFOLD FOR
REVERSIBLE HYDROGEN STORAGE. THESIS ADVISOR :
ASST. PROF. RAPEE GOSALAWIT-UTKE, Ph.D. 84 PP.

HYDROGEN STORAGE/NANOCONFINEMENT/LITHIUM BOROHYDRIDE/
MAGNESIUM HYDRIDE/CARBON AEROGEL SCAFFOLD

Light metal hydrides are the favored materials for solid hydrogen storage applications. However, they have slow hydrogen sorption kinetics and high thermodynamic stability. To improve these disadvantages, the concept of reactive hydride composite (RHC) is modified. Among composite hydrides, lithium borohydride (LiBH₄) combined with magnesium hydride (MgH₂) shows an enhancement of hydrogen sorption properties. For the formation of MgB₂ compound upon dehydrogenation, the de/rehydrogenation enthalpy is lower than pure LiBH₄ according to $2\text{LiBH}_4 + \text{MgH}_2 \leftrightarrow \text{LiH} + \text{MgB}_2 + 4\text{H}_2$. Although the reaction enthalpy is lower, desorption and absorption processes occur at high temperature with relatively slow two step kinetics. To improve the disadvantages of LiBH₄ - MgH₂ system, the nanoconfinement by the melt infiltration into inert carbon aerogel scaffold (CAS) of metal hydrides are focused as it benefits for many aspects: increased of surface area and grain boundaries and nanoscale diffusion distances, which then facilitate the release and the uptake of hydrogen and enhance reaction kinetics. On the other hand, the nanoconfinement in nanoporous carbon aerogel scaffolds causes the disadvantages of high pressure and temperature for de/rehydrogenation. In this study,

we prepared the nanoconfined RHCs by melt infiltration of nanoconfined 2LiBH_4 -premilled MgH_2 into CAS. We also reduced the particle size of MgH_2 for better nanoconfinement. The weight ratio of the composite hydride ($2\text{LiBH}_4\text{-MgH}_2$): CAS was decreased from the previous work (from 2:1 to 1:1) to enhance the hydrogen storage capacity of the systems. The N_2 adsorption-desorption and SEM-EDS-mapping was carried out to confirm the nanoconfinement of both LiBH_4 and MgH_2 . Nanoconfined 2LiBH_4 -premilled MgH_2 revealed only one step dehydrogenation at $345\text{ }^\circ\text{C}$ without B_2H_6 release whereas that of nanoconfined sample without MgH_2 premilling reveals several steps at high temperature (up to $430\text{ }^\circ\text{C}$) with B_2H_6 release. With the premilling process, the activation energy (E_A) was reduced to 16.8-138 kJ/mol. Significant dehydrogenation temperature of nanoconfined $2\text{LiBH}_4\text{-MgH}_2$ is achieved at the lowest temperature ($T = 320\text{ }^\circ\text{C}$) when compared with other modified $2\text{LiBH}_4\text{-MgH}_2$ systems.

School of Chemistry

Academic Year 2013

Student's Signature_____

Advisor's Signature_____

ACKNOWLEDGEMENTS

I wish to thank my advisor Asst. Prof. Dr. Rapee Gosalawit-Utke for her endless patience, support, guidance, and advice provided over the course of my thesis. I would also like to thank the thesis examining committee, including Assoc. Prof. Dr. Jatuporn Wittayakun, Asst. Prof. Dr. Sanchai Prayoonpokarach, and Asst. Prof. Dr. Kulawadee Rungsriwatananon for their helpful and suggestions during my thesis defense. I would like to thank my friends, Nuntida Wiset, Praphatson Plerdsranoy, and Sukanya Meethom for constant support throughout the learning process and encouragement.

I would to acknowledge the Institute of Research and Development SUT for financial support. I also would like to thank Dr. Yanling Hua (The Centre for Scientific and Technological Equipment, Suranaree University of Technology, Thailand) for technical help and suggestions during solid-state ^1H and ^{11}B MAS NMR measurements. Last, I would also like to thank my family for their encouragement and moral support in every step of my academic career.

Sophida Tiangwiriya

CONTENTS

	Page
ABSTRACT IN THAI.....	I
ABSTRACT IN ENGLISH	III
ACKNOWLEDGEMENTS.....	V
CONTENTS.....	VI
LIST OF TABLES	IX
LIST OF FIGURES	X
CHAPTER	
I INTRODUCTION.....	1
1.1 Hydrogen energy.....	1
1.2 Hydrogen production	2
1.3 Hydrogen fuel cell.....	4
1.4 Hydrogen storage systems	7
II LITERATURE REVIEWS.....	11
2.1 Properties of LiBH_4	12
2.1.1 Structural properties of LiBH_4	12
2.1.2 Decomposition of LiBH_4	12
2.2 Thermodynamics.....	13
2.3 Kinetics	15
2.4 LiBH_4 based material for hydrogen storage.....	17

CONTENTS (Continued)

	Page
2.4.1 Additive and catalytic doping	17
2.4.2 Reactive hydride composites.....	20
2.4.3 Nanoconfinement	22
2.4 Research objectives.....	30
III EXPERIMENTAL	31
3.1 Chemicals and materials	31
3.2 Apparatus	32
3.2.1 Glove box	32
3.2.2 Ball mill.....	32
3.3 Instruments.....	33
3.4 Sample preparation.....	33
3.4.1 Synthesis of carbon aerogel scaffold.....	33
3.4.2 Ball milling of metal hydrides.....	35
3.4.3 Melt infiltration	36
3.5 Sample characterizations.....	36
3.5.1 N ₂ adsorption-desorption.....	36
3.5.2 Scanning Electron Microscopy (SEM) and Energy Dispersive X-ray Spectroscopy (EDS) mapping.....	36
3.5.3 Simultaneous Thermal Analysis (STA) and Mass Spectroscopy (MS).....	37

CONTENTS (Continued)

	Page
3.5.4 In situ Synchrotron Radiation Powder X-ray Diffraction (SR-PXD)	37
3.5.5 Fourier Transform Infrared Spectrometry (FTIR).....	37
3.5.6 Magic Angle Spinning Nuclear Magnetic Resonance (MAS-NMR) measurement.....	38
3.5.7 Sievert-Type apparatus.....	38
IV RESULTS AND DISCUSSION.....	41
4.1 Melt infiltration	41
4.2 Dehydrogenation and reaction mechanisms.....	46
4.3 Kinetics, reversibility, and hydrogen reproducibility	54
V CONCLUSION.....	63
REFERENCES	64
APPENDICES	72
APPENDIX A CALCULATON FOR SYNTHESIS OF CARBON AEROGEL SCAFFOLD AND HYDROGEN STORAGE CAPACITY	73
APPENDIX B DATA FOR CALCULATON OF ACTIVATION ENERGY.....	77
APPENDIX C SCHEMATICC DIAGRAM OF SIEVERT-TYPE APPARATUR.....	82

CONTENTS (Continued)

	Page
CURRICULUM VITAE.....	84



LIST OF TABLES

Table	Page
1.1 Types of Fuel Cells	6
1.2 Comparison of three major competing technologies for hydrogen Storages.....	7
1.3 Development of specific technical targets in 2015 by DOE and FreedomCAR Hydrogen Storage Team.....	10
3.1 Chemicals and materials used in this work.....	31
4.1 Texture parameter of CAS, nanoconfined 2LiBH_4 - MgH_2 and nanoconfined 2LiBH_4 -premilled MgH_2 from N_2 sorption measurements	42

LIST OF FIGURES

Figure	Page
1.1 Hydrogen cycle	2
1.2 Hydrogen Fuel cell.....	5
1.3 Schematic working of Hydrogen Fuel cell stack	5
1.4 Compressed hydrogen gas tank	8
1.5 Liquid hydrogen storage tank	9
1.6 Solid-state hydride thanks of NaAlH ₄	10
2.1 Stored hydrogen per mass and per volume of metal hydrides, carbon nanotubes, petrol, and other hydrocarbons	11
2.2 Crystal structure of LiBH ₄ phase	12
2.3 Thermal desorption spectra of LiBH ₄	13
2.4 Pressure-composition isotherms	14
2.5 Activation energy (EA) and enthalpy (ΔH) diagram	16
2.6 Comparison of the modified LiBH ₄ materials with the commercial LiBH ₄	18
2.7 Temperature programmed hydrogen release profiles for pure LiBH ₄ and LiBH ₄ doping with various additive	18
2.8 Comparison on the first dehydrogenation between LiBH ₄ and grapgene.....	19
2.9 Enthalpy diagram for the destabilization of LiBH ₄ by MgH ₂	20
2.10 Temperature dependence of dehydrogenation for 6LiBH ₄ -SrH ₂	22

LIST OF FIGURES (Continued)

Figure	Page
2.11 Volumetric measurement of dehydrogenation of LiBH ₄ /aerogel and LiBH ₄ /graphite	23
2.12 DSC traces of bulk LiBH ₄ , physically mixed LiBH ₄ /NPC, and pre-melted LiBH ₄ @NPC	24
2.13 Isothermol dehydrogenation curves of LiBH ₄ /SBA-15 at deference temperatures	25
2.14 DSC, TGA, and MS showing the hydrogen release reactions from nanoconfined and bulk 2LiBH ₄ -MgH ₂ . nanoconfined 2LiBH ₄ -MgH ₂ and bulk 2LiBH ₄ -MgH ₂	26
2.15 Normalized hydrogen desorption profiles of the nanoconfined 2LiBH ₄ -MgH ₂ and bulk 2LiBH ₄ -MgH ₂	28
2.16 Kissinger plots representing the activation energy (E _A) of MgH ₂ and LiBH ₄ dehydrogenation of bulk and nanoconfined samples.....	29
3.1 Glove box use in the laboratory	32
3.2 a Spex 8000 M Mixer/Mill and Tungsten carbide vialset.....	32
3.3 Reaction mechanisms during cross-linked polymerized.....	34
3.4 The gel formation in the resorconal-formaldehyde system	35
3.5 Sievert-type apparatus assembled in the Chemistry Laboratory.....	39
4.1 SEM images and elemental analysis (EDS result) of nanoconfined 2LiBH ₄ -MgH ₂ and nanoconfined 2LiBH ₄ -premilledMgH ₂	44

LIST OF FIGURES (Continued)

Figure	Page
4.2 SEM micrograph and elemental mapping mode of nanoconfined $2\text{LiBH}_4\text{-MgH}_2$	45
4.3 SEM micrograph and elemental mapping mode of nanoconfined $2\text{LiBH}_4\text{-premilled MgH}_2$	45
4.4 Simultaneously performed DSC, TGA, and Mass spectrometry of the hydrogen release reactions from nanoconfined $2\text{LiBH}_4\text{-MgH}_2$ and the nanoconfined $2\text{LiBH}_4\text{-premilled MgH}_2$	47
4.5 Schematic draw of the process for nanoconfined $2\text{LiBH}_4\text{-MgH}_2$ and nanoconfined $2\text{LiBH}_4\text{-premilled MgH}_2$	49
4.6 SR-PXD spectra of the nanoconfined $2\text{LiBH}_4\text{-premilled MgH}_2$ during dehydrogenation.....	51
4.7 FT-IR spectrum of nanoconfined $2\text{LiBH}_4\text{-premilled MgH}_2$, nanoconfined $2\text{LiBH}_4\text{-premilled MgH}_2$ after dehydrogenation, and after rehydrogenation	52
4.8 ^1H MAS NMR spectra of pure LiBH_4 , nanoconfined $2\text{LiBH}_4\text{-premilled MgH}_2$ after rehydrogenation and pure MgH_2	53
4.9 ^{11}B MAS NMR spectra of pure LiBH_4 and nanoconfined $2\text{LiBH}_4\text{-premilled MgH}_2$ after absorption	54
4.10 DSC curves with deconvolution for several heating rate of nanoconfined $2\text{LiBH}_4\text{-MgH}_2$ and the Kissinger plot representing the activation energy	56

LIST OF FIGURES (Continued)

Figure	Page
4.11	DSC curves with deconvolution for several heating rate of nanoconfined 2LiBH ₄ -premilled MgH ₂ and the Kissinger plot representing the activation energy 57
4.12	The hydrogen desorption profile of nanoconfined 2LiBH ₄ -MgH ₂ and nanoconfined 2LiBH ₄ -premilled MgH ₂ 59
4.13	Simultaneously performed DSC and Mass spectrometry of the nanoconfined 2LiBH ₄ -premilled MgH ₂ after rehydrogenation 60
4.14	¹¹ B MAS NMR spectra of pure LiBH ₄ , nanoconfined 2LiBH ₄ -premilled MgH ₂ after rehydrogenation and after 2 nd dehydrogenation at 300 °C for 1h 61
4.15	¹ H MAS NMR spectra of pure LiBH ₄ , nanoconfined 2LiBH ₄ -premilled MgH ₂ after rehydrogenation, after 2 nd dehydrogenation at 300 °C for 1h and pure MgH ₂ 62

CHAPTER I

INTRODUCTION

1.1 Hydrogen Energy

Hydrogen is regarded as one of the best alternative energy carriers due to the following reasons: (i) hydrogen is the most abundant element on earth, comprising about three-quarters of the mass of the universe, (ii) among all elements, hydrogen owns the highest ratio of valence electrons to proton (and neutron), resulting in high energy storage per electron, (iii) it diffuses immediately upwards into the air and does not pollute the ground or groundwater, (iv) hydrogen does not produce acid rain, deplete the ozone layer, or produce harmful emissions, and (v) use of hydrogen as a fuel is renewable. The gravimetric energy density of hydrogen ($33.33 \text{ kWh kg}^{-1}$) is approximately three times higher than gasoline (12.7 kWh kg^{-1}). However, the low volumetric energy density of hydrogen (0.77 kWh l^{-1} at 35 MPa and 25 °C) in comparison with gasoline (8.76 kWh l^{-1}) is the reason for the increased package volume required for a hydrogen storage system compared with conventional gasoline/diesel fuel systems (Stolen., 2010). A typical hydrogen cycle (Züttel *et al.*, 2008), shown in Figure 1.1 consists of three major steps, which are hydrogen production from renewable energy sources, transportation and storage of the hydrogen, and its use in fuel cell to produce energy. Each of these steps is associated

with significant technical challenges that must be solved before the benefits of using hydrogen as an energy carrier can be fully realized.

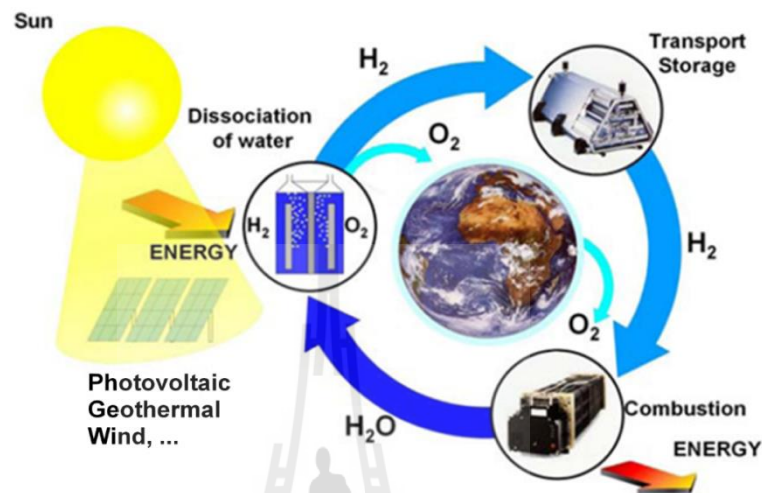


Figure 1.1 Hydrogen cycle (Züttel *et al.*, 2008).

1.2 Hydrogen production

1.2.1 Natural gas reforming

Hydrogen can be produced from natural gas using high-temperature steam. To separate hydrogen from carbon components in methane and methanol, this method is the cheapest, most efficient, and most common for producing hydrogen. Steam reforming uses thermal energy to separate hydrogen from the carbon components in methane and methanol and involves the reaction of these fuels with steam on catalytic surfaces. The first step of the reaction is the decomposition of the fuel into hydrogen and carbon monoxide. Then a shift reaction changes the carbon monoxide and water to carbon dioxide and hydrogen. These reactions occur at temperatures of 200 °C or greater.

1.2.2 Renewable electrolysis

Electrolysis separates the element of water (hydrogen (H) and oxygen (O)). If the electricity is from renewable sources, such as solar and wind, the resulting hydrogen will be considered renewable.

1.2.3 Gasification

Gasification is a process, in which coal or biomass is converted into gaseous components by applying heat under pressure of air/oxygen and steam. The resulting synthesis gas contains hydrogen and carbon monoxide, which are reacted with steam to produce more hydrogen.

1.2.4 Nuclear high-temperature electrolysis

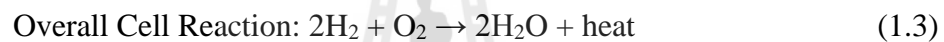
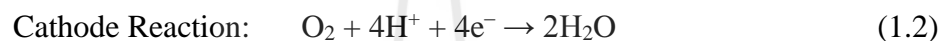
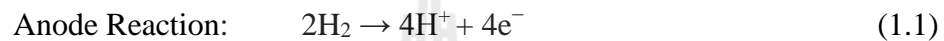
Heat from a nuclear reactor can be used to improve the efficiency of water electrolysis to produce hydrogen. By increasing the temperature of the water, less electricity is required to split it into hydrogen and oxygen, which reduces the total energy required.

1.2.5 Biological and photoelectrochemical

Biological and photobiological processes use algae and bacteria to produce hydrogen. Under specific conditions, the pigments in certain types of algae absorb solar energy. The enzymes in the cell act as a catalyst to split the water molecules. Some bacteria are also capable of producing hydrogen, but unlike algae they require a substrate to grow on. The organisms not only produce hydrogen, but also can clean up pollution (Riis *et al.*, 2006; Léon., 2008; and Freedom CAR & Fuel Partnership, www, 2009).

1.3 Hydrogen fuel cells

A fuel cell is an electrochemical cell, i.e., a device in which a chemical process is converted the chemical energy of hydrogen directly into electrical and thermal energy. It has two electrodes, an anode (negative) and a cathode (positive), separated by a membrane, giving an overall electrochemical reaction (equation 1.1, 1.2, and 1.3) (Hydrogen fuel cell, www, 2014).



Oxygen passes over one electrode and hydrogen over the other. Hydrogen reacts with a catalyst on the anode and converts into negatively charged electrons (e^-) and become to a positively charged called proton (H^+). The electrons flow out of the cell to be used as electrical energy. The protons move through the electrolyte membrane to cathode, where electrons and protons combine with oxygen to produce water as show in Figure 1.2. To get higher energy, the individual fuel cells are combined into a fuel stack (Figure 1.3), which is done efficiently by connecting each cell to the next. The continuous operation of the stack requires effective heat, air, hydrogen, and water management enable by auxiliary equipment such as pumps and blowers.

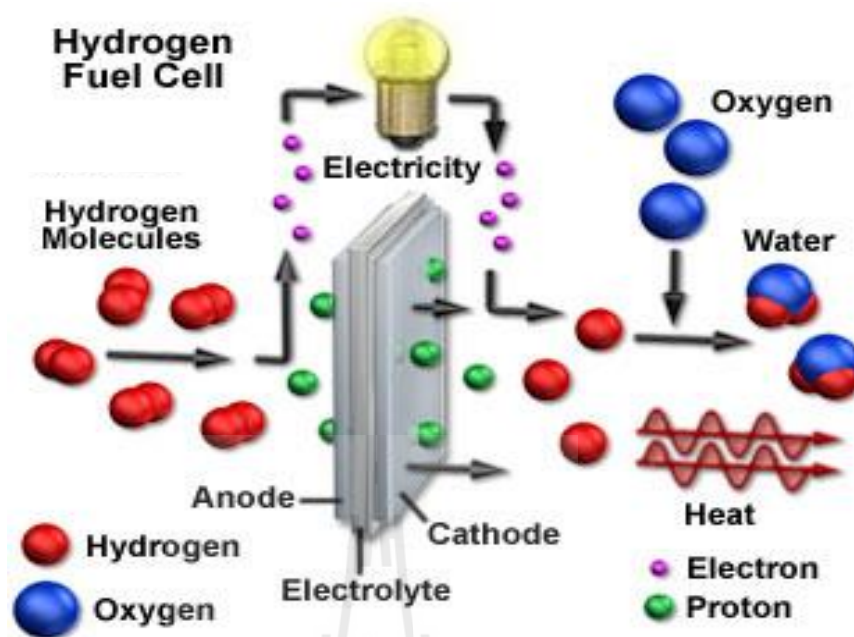


Figure 1.2 Hydrogen fuel cell. (<http://micro.magnet.fsu.edu/primer/java/fuelcell/>).

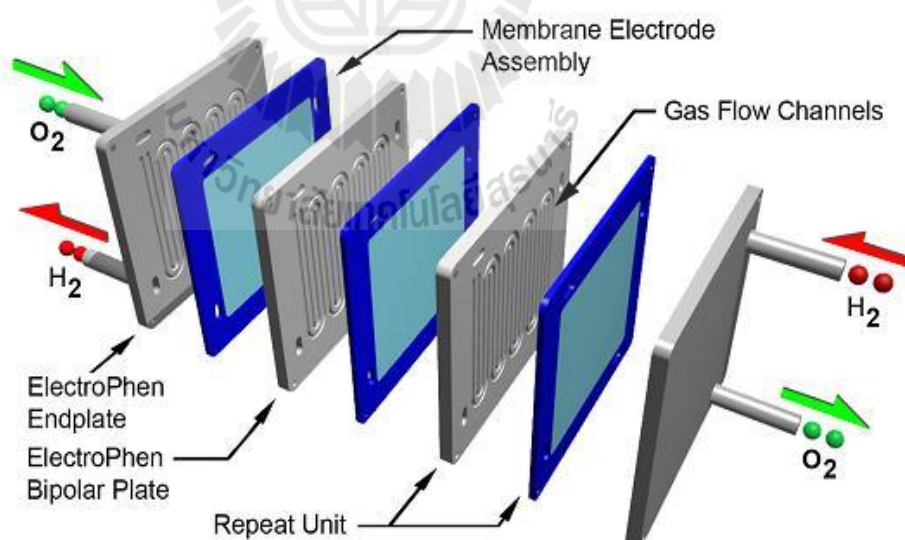


Figure 1.3 Schematic working of hydrogen fuel cell stack (<http://www.futureenergies.com/modules.php?op=modload&name=News&file=article&sid=959>).

Fuel cell types are characterized by their electrolytes, cost, efficiency, and temperature of operation. There are six different types of fuel cells (Table 1.1): (1) alkaline fuel cell (AFC), (2) direct methanol fuel cell (DMFC), (3) molten carbonate fuel cell (MCFC), (4) phosphoric acid fuel cell (PAFC), (5) proton exchange membrane fuel cell (PEMFC), and (6) solid oxide fuel cell (SOFC).

Table 1.1 Types of Fuel Cells (Guta, 2008).

	AFC	DMFC	MCFC	PAFC	PEMFC	SOFC
electrolyte	Potassium hydroxide	Polymer membrane	Immobilized liquid molten carbonate	Immobilized liquid phosphoric acid	Ion exchange membrane	Ceramic
Operating temperature (°C)	60-90	60-130	650	200	80	1000
Efficiency (%)	45-60	40	45-60	35-40	40-60	50-65
Typical electrical power	Up to 20 kW	<10 kW	>1MW	>50 kW	Up to 250 kW	>200 kW
Possible application	ubmarines, spacecraft	Portable applications	Power stations	Power stations	Vehicles, small station	Power stations

The proton exchange membrane (PEM) fuel cell is the most suitable system for transportation application because of its relatively low operating temperature (about 80 °C), high power density, rapid change in power on demand, and quick start-up. Moreover, PEM fuel cells are being used more and more in stationary applications

in the last five years. In order to use PEM fuel cells efficiently, high hydrogen storage capacity materials are considerably required.

1.4 Hydrogen storage systems

There are three major competing technologies for hydrogen storages: compressed hydrogen gas, liquid hydrogen tanks, and solid state hydrides.

Table 1.2 Comparison of three major competing technologies for hydrogen storages (Varin *et al.*, 2009).

Storage system	Volumetric hydrogen capacity ($\text{kgH}_2 \text{ m}^{-3}$)	Drawbacks
Compressed hydrogen gas under 80 MPa pressure	~40	-Safety problem -cost of pressurization; -large pressure drop during use
Liquid hydrogen at cryogenic temperature of $-252\text{ }^\circ\text{C}$ (21 K)	~71	-Large thermal losses -safety -cost of liquefaction
Solid state hydrides	80–160	-None of the above

Compressed hydrogen is the gaseous state of hydrogen, storing at high pressure (~80 MPa). This system requires further research and development on materials and techniques due to safety concerns. Regarding the large pressure drop during use and high cost of production, this system still cannot reach the target for

hydrogen storage application. The high compressed gas system includes cylindrical tanks as shown in Figure 1.4.

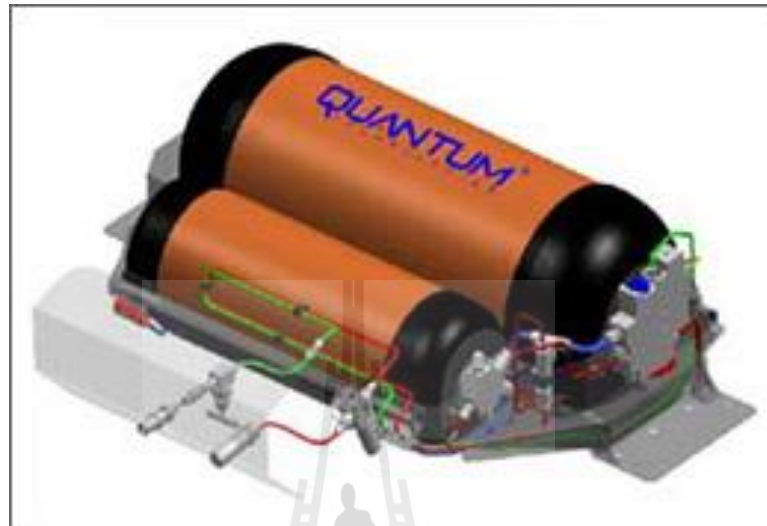


Figure 1.4 Compressed hydrogen gas tank (http://www.physics.oregonstate.edu/~demareed/313Wiki/doku.php?id=nanotube_based_hydrogen_storage).

In the case of liquid state, hydrogen is stored in the cryogenic tank ($-252\text{ }^{\circ}\text{C}$) and under pressure (0.2-1.0 MPa) as shown in Figure 1.5. Due to very low temperature and pressure in the tank, it is very important to avoid external heat from the system. The major drawbacks of liquid storage are cost of liquefaction and large thermal losses for open system. However, liquid hydrogen tanks can store more hydrogen in a given volume than compressed gas tank.



Figure 1.5 Liquid hydrogen storage tank (<http://green.autoblog.com/2009/05/15/first-czech-hydrogen-station-to-open-in-the-fall>).

For solid-state hydrides, hydrogen can be stored in several pathways, such as metal hydrides, intermetallic hydrides, and complex hydrides. Hydrogen can be stored either on the surface of solids (by adsorption) or within solids (by absorption). Hydrogen stored in the form of solid-state hydride is higher quantity in the smaller volume at moderate temperature and pressure as compared with those two storages of compressed and liquid hydrogen. Moreover, this system is claimed to store hydrogen in high purity, thus, it can be used directly to supply hydrogen to PEM fuel cells, attractive fuel cell systems for mobile application in the future. In addition, as a hydrogen storage (Figure 1.6) containing sodium aluminum hydride (NaAlH_4), one of the most attractive complex hydrides for solid-state hydrogen storage, it is obviously compact as compared with those two systems mentioned previously.



Figure 1.6 Solid-state hydride tanks of NaAlH₄ (capacity 8 kg NaAlH₄, ca. 400 gH₂).
(<http://www.flyhy.eu/HZG.html>, 2013).

The DOE and Freedom CAR Hydrogen Storage Team developed specific technical targets to consider a prospective compound as a hydrogen storage system.

Table 1.3 Development of specific technical targets in 2015 by DOE and Freedom CAR Hydrogen Storage Team (Varin *et al.*, 2009).

Targeted factors	Year 2015
Specific energy (MJ/kg)	10.8
Gravimetric capacity (wt.%)	9
Volumetric capacity (kg H ₂ /m ⁻³)	81
Operating temperature (°C)	-40/60
Cycle life (cycle)	1500
Delivery pressure (bar)	2.5

CHAPTER II

LITERATURE REVIEWS

Among all hydride materials, lithium borohydride (LiBH_4) is well-known as one of the most prominent solid-state metal complex hydrides for reversible hydrogen storage applications, due to its high volumetric (121 kg/m^3) and gravimetric hydrogen densities (18.5 mass %). From Figure 2.1, LiBH_4 shows the most suitable gravimetric and volumetric hydrogen densities at moderate temperature (Züttel *et al.*, 2003).

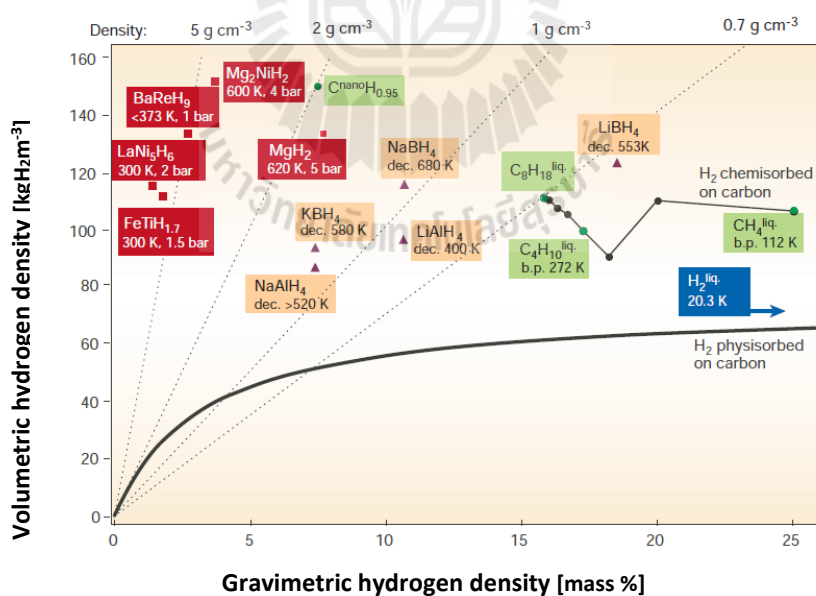


Figure 2.1 Stored hydrogen per mass and per volume of metal hydrides, carbon nanotubes, petrol, and other hydrocarbons (Züttel *et al.*, 2003).

2.1 Properties of LiBH₄

2.1.1 Structural properties of LiBH₄

For the structural properties of LiBH₄, the low temperature structure of LiBH₄ is *Pnma*, and experimental high temperature structure is *P6₃mc*. At room temperature and under high pressure, LiBH₄ forms *Ama2* and *Fm-3m* structures as shown in Figure 2.2 (Li *et al.*, 2011).

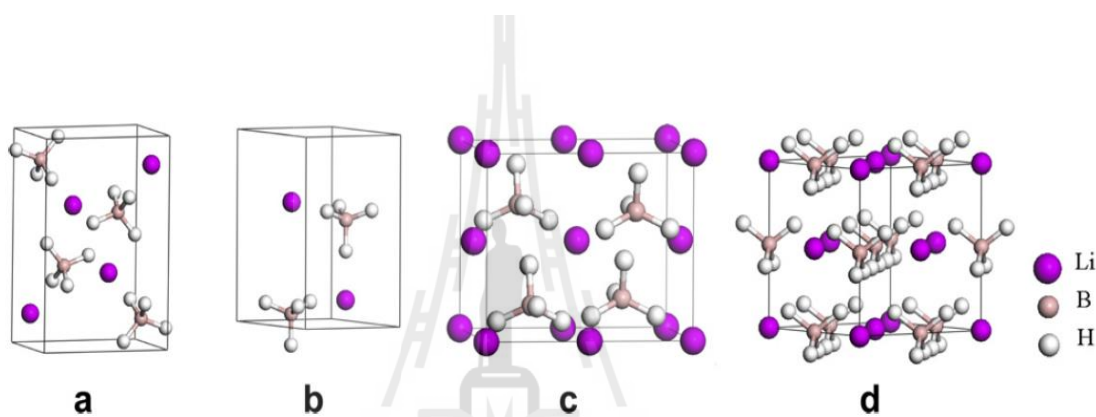
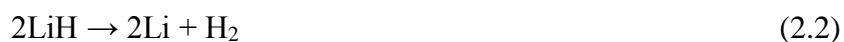


Figure 2.2 Crystal structure of LiBH₄ : *Pnma* (a), *P6₃mc* (b), *Ama2*, and *Fm-3m* (d) (Li *et al.*, 2011).

2.1.2 Decomposition of LiBH₄

LiBH₄ is thermodynamically very stable due to its strong covalent bond in borohydride [BH₄]⁻ structure. The enthalpy change (ΔH) for dehydrogenation is 67 kJ/mol. The dehydrogenation of LiBH₄ is divided into two steps as shown in reaction 2.1 and 2.2, respectively. Afterward, rehydrogenation can be obtained as shown in reaction (2.3) (Orimo *et al.*, 2005).





The thermal desorption spectra of pure LiBH_4 shown in Figure 2.3 exhibits slight hydrogen desorption between 100 and 200 °C of 0.3 wt. %. The peaks at 110 and 280 °C are the structural phase transformation and the melting point of LiBH_4 , respectively. At 320 °C, the first significant hydrogen desorption peak starts and liberates an additional 1 wt. % of hydrogen. The first desorption goes over to a second desorption peak starting at 400 °C and reaches its maximum around 500 °C. (Züttel *et al.*, 2003).

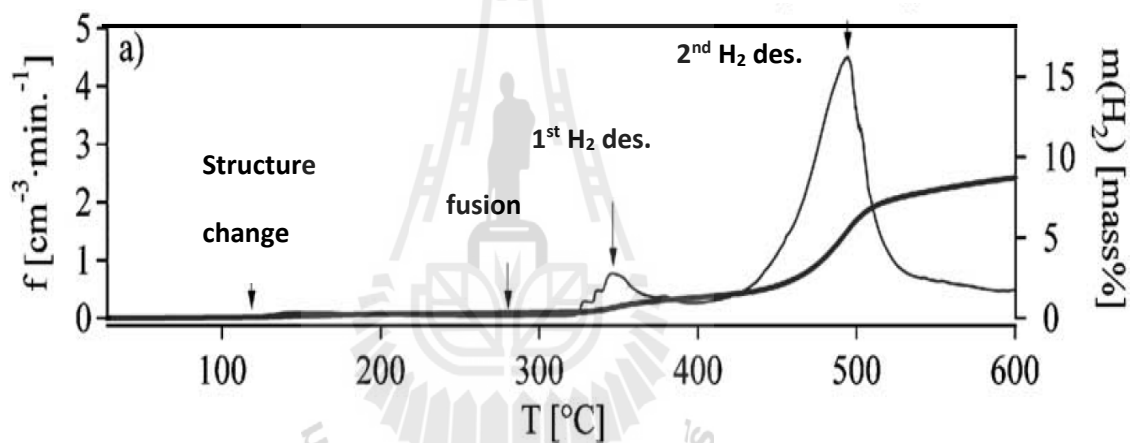


Figure 2.3 Thermal desorption spectra of LiBH_4 . The sample was heated after evacuation at room temperature with a heating rate of 2 °C/min. The gas flow was measured as a function of time and the desorbed hydrogen was computed from the integrated gas flow (Züttel *et al.*, 2003).

2.2 Thermodynamics

A hydride-forming metal (M) will form metal hydride when it is exposed to hydrogen (reaction (2.4)).



Where Q is the heat of reaction of hydride formation. The thermodynamic aspect of this reaction can be described by pressure-composition isotherms (PCI). A schematic PCI curve is shown in Figure 2.4 (Hirscher., 2010)

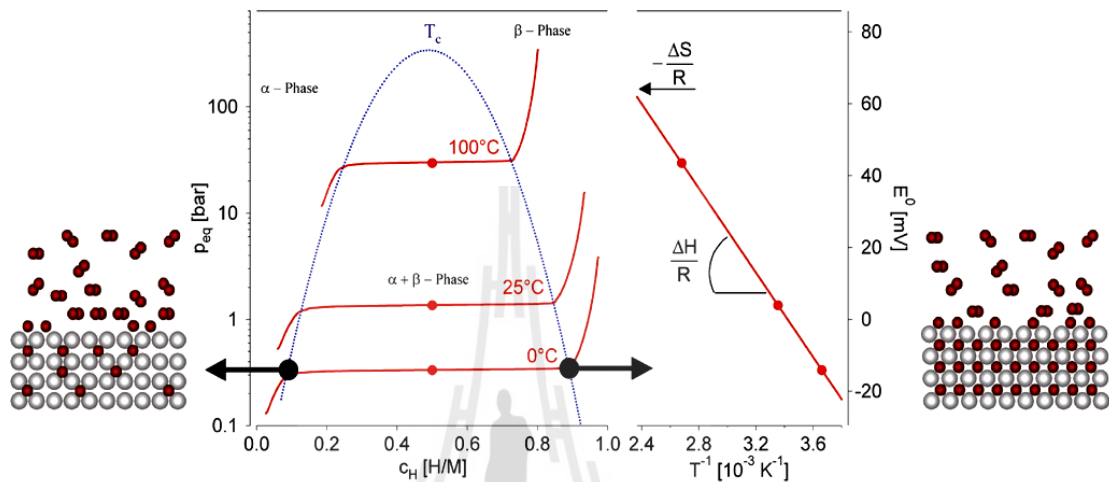


Figure 2.4 Pressure-composition isotherms, α is the solid solution of hydrogen (α -phase) and β is the hydride phase (β -phase), and corresponding Van't Hoff plot giving the enthalpy of hydride formation ΔH ([http://students.chem.tue.nl/ifp14/Metal hydrides.htm](http://students.chem.tue.nl/ifp14/Metal%20hydrides.htm)).

From Figure 2.4, when hydrogen comes into contact with a hydride-forming metal, the hydrogen molecules (H_2) firstly physisorb on the surface and they then dissociate into two hydrogen atoms ($2H$), which can diffuse into the metal and forming a solid solution of hydrogen atoms dissolved in the metal lattice. This is usually referred to the α -phase, which has the same crystal structure as the bare metal. As the hydrogen pressure increases, the concentration of hydrogen atom dissolved into the metal in equilibrium with the gas phase also increases. When the concentration exceeds a

certain critical value, where the attractive M-H interaction become important, a higher concentration phase (β -phase) starts to form. The system now has three phases (α , β , and hydrogen gas) and components (metal and hydrogen). This transition from the α - to β -phase is equilibrium. The equilibrium pressure P_{eq} as a function of temperature is related to the changes of enthalpy (ΔH) and entropy (ΔS) by the Van't Hoff equation (equation 2.5),

$$\ln(P_{eq}/P_0) = \Delta H/RT - \Delta S/R \quad (2.5)$$

where P_{eq} is the plateau pressure, T is the temperature, P_0 is reference pressure (1 bar), R is the gas constant ($R = 8.314 \text{ J/mol.K}$), ΔH and ΔS are the enthalpy and entropy changes, respectively, occurring during the $\alpha \rightarrow \beta$ transformation. The transition from α - to β -phase, determined by the enthalpy and entropy of the formation of the hydride, is therefore a very important character of any potential metal hydride forming material. For practical applications, the pressures, at which this transition takes place, must be close to 1 bar at relatively low temperature ($\sim 100 \text{ }^\circ\text{C}$). Assuming that ΔS is the entropy of gaseous hydrogen ($130 \text{ Jmol}^{-1}\text{K}^{-1}$), the enthalpy of formation of the hydride (ΔH) should be between -30 and -55 kJmol^{-1} to achieve 1 bar H_2 equilibrium between 40 - $150 \text{ }^\circ\text{C}$, based on the Van't Hoff equation, (Zütter *et al.*, 2008). Unfortunately, none of the hydrides with sufficiently high hydrogen content has the desired thermodynamic properties.

2.3 Kinetics

Not only thermodynamic factors, but also the slow sorption kinetics is an obstacle to practical application for metal hydrides. A metal hydrogen system is

required to rapidly absorb and desorb hydrogen at moderate temperature. The rate of many chemical reactions is dominated by the presence of activation barriers in the reaction pathway. The H_2 absorption and desorption of many compounds are chemical reactions, which show significantly high activation barriers. Figure 2.5 shows a typical activation barrier for a generic system, where the activation energy, E_a , quantifies the value of the barrier.

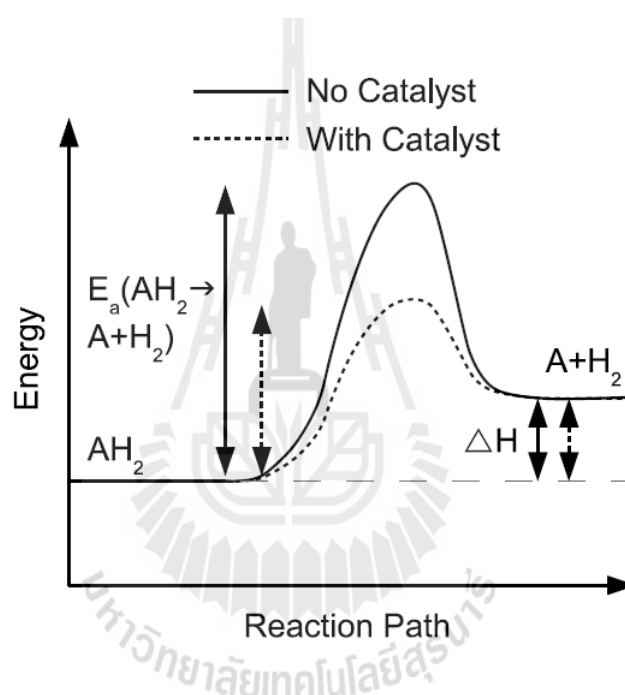


Figure 2.5 Activation energy (E_A) and enthalpy (ΔH) diagram of the reaction $AH_2 \leftrightarrow A + H_2$ (http://commons.wikimedia.org/wiki/File:Activation_energy.svg).

Figure 2.5 also shows the effect of catalyst on the system. Addition of catalyst has no effect on the thermodynamics of the system as the nature of the reactants and products (i.e., ΔH) is unchanged, but the activation energy is reduced.

The Kissinger analysis can be employed to measure the activation energy of the reaction from experimental differential scanning calorimetry (DSC). The method

developed by Kissinger allows for obtaining the activation energy of a chemical reaction of any order by considering the variation of the peak temperature. The Kissinger analysis can be described in the equation (2.6)

$$\ln(\beta_{\text{ramp}}/T_{\text{max}}^2) = -E_A/RT_{\text{max}} + \ln(k_0) \quad (2.6)$$

where β is the heating rate ($^{\circ}\text{C}/\text{min}$), T_{max} is the temperature of desorption, R is the gas constant ($8.314 \text{ J mol}^{-1} \text{ K}^{-1}$), E_A is the activation energy, and k_0 is a constant. The activation energy calculated from the slope of the plot of $\ln(\beta_{\text{ramp}}/T_{\text{max}}^2)$ versus $1/T_{\text{max}}$.

2.4 LiBH₄ based materials for hydrogen storages

Many strategies, i.e., additive and catalytic doping, reactive composite hydrides, and nanoconfinements, have been carried out to especially decrease de/rehydrogenation temperature as well as kinetic and thermodynamic improvement. For example:

2.4.1 Additive and catalytic doping

Au *et al.* (Au *et al.*, 2006) modified LiBH₄ by ball milling with metal oxides and metal chlorides (TiO₂, TiCl₃, ZrO₂, V₂O₃, and SnO₂). It was found that dehydrogenation rate was improved at lower temperature with respect to commercial LiBH₄ as shown in Figure 2.6. The materials of 75% LiBH₄+25% TiO₂, 75% LiBH₄+25% V₂O₂, 75% LiBH₄+25% ZrO₂, 75% LiBH₄+25% SnO₂, and 75% LiBH₄+25% TiCl₃ desorbed 8-9 wt. % hydrogen in the temperature range of 175 to 200 $^{\circ}\text{C}$. Later, Xu *et al.* (Xu *et al.*, 2013) also reported enhancement of dehydrogenation and rehydrogenation properties of LiBH₄ by doping with graphene and other carbon materials. It was observed that the onset dehydrogenation

temperature of LiBH_4 is reduced from 420 °C (for pure LiBH_4) to 320, 280, 280, and 230 °C by doping with 20 wt. % of Vulcan C, carbon nanotube, BP2000, and grapheme, respectively (Figure 2.7).

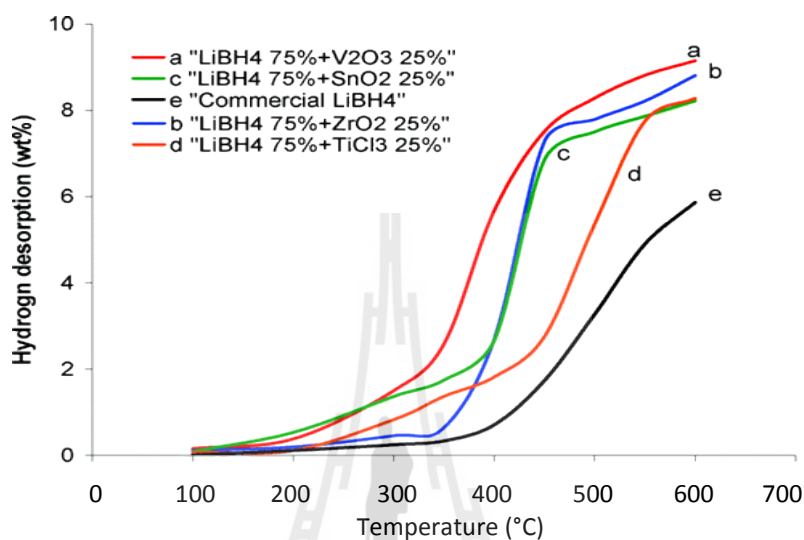


Figure 2.6 Comparison of the modified LiBH_4 materials with the commercial LiBH_4 (Au *et al.*, 2006).

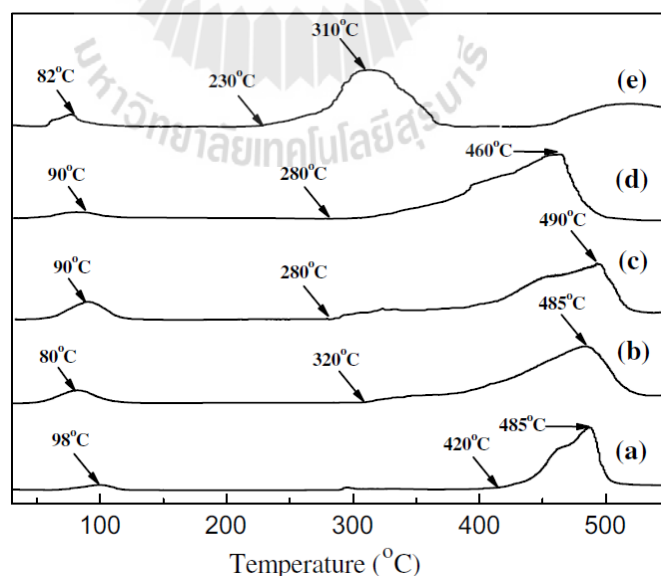


Figure 2.7 Temperature programmed hydrogen release profiles for pure LiBH_4 (a), and LiBH_4 doped with Vulcan C (b), carbon nanotube (c), BP2000 (d), and graphene (e) (Xu *et al.*, 2013).

From the results, they found that the reduction of onset dehydrogenation temperature probably came from distinct specific surface area and suitable pore distribution. Noticeably, among these carbon additives, graphene revealed the best catalytic effect on the decomposition of LiBH_4 . Dehydrogenation kinetics of LiBH_4 doped with graphene at $450\text{ }^\circ\text{C}$ under 3-4 bar H_2 were studied and compared with pure LiBH_4 . Within 90 min, pure LiBH_4 release only 4.3 wt. % hydrogen, while LiBH_4 doping with graphene release up to 9.2 wt. % hydrogen. Evidently, graphene possessed a promoting effect on the dehydrogenation amount and kinetics of LiBH_4 .

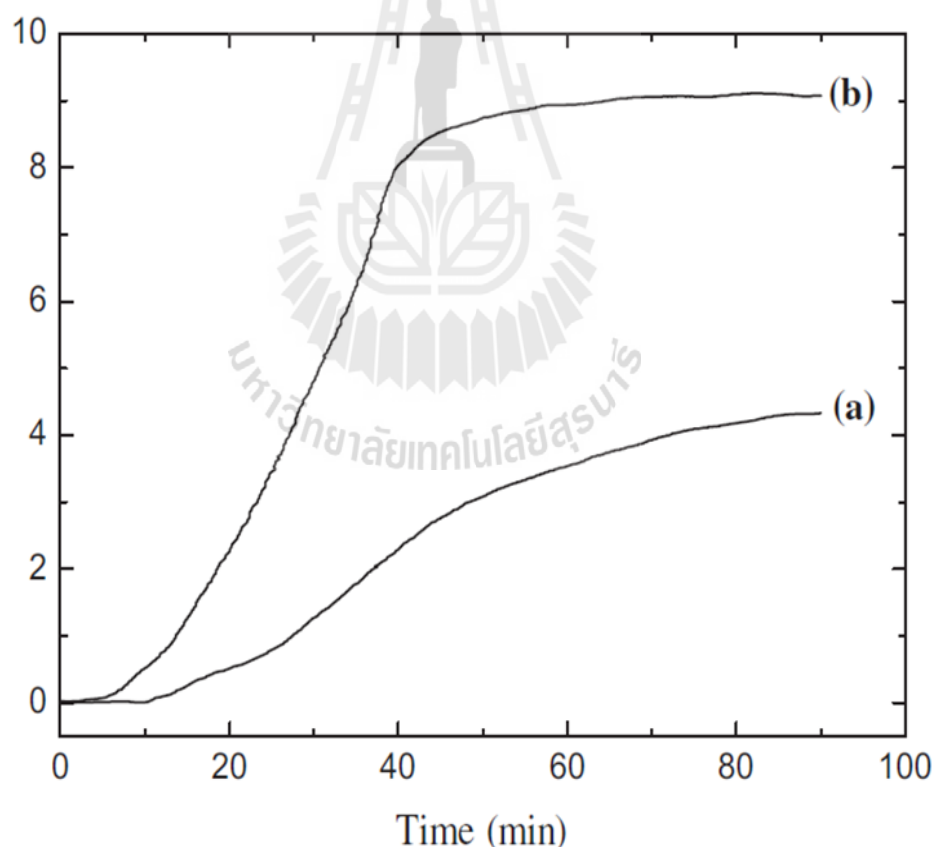


Figure 2.8 Comparison on the first dehydrogenation curves between the pure LiBH_4 (a) and 20 wt. % graphene doped LiBH_4 (b) at $450\text{ }^\circ\text{C}$ under 3-4 bar H_2 (Xu *et al.*, 2013).

2.4.2 Reactive hydride composites

Thermodynamic destabilization is successfully achieved by combining LiBH_4 with reactive additives that form metal borides instead of boron upon dehydrogenation. Such event can decrease the overall enthalpy for dehydrogenation and increase the equilibrium hydrogen pressure. Vajo *et al.* (Vajo *et al.*, 2005, 2007) destabilized LiBH_4 by MgH_2 doping with a molar ratio of 2:1 ($\text{LiBH}_4:\text{MgH}_2$). They found that desorption enthalpy and temperature of the $2\text{LiBH}_4\text{-MgH}_2$ composition decreased to 46 kJ/molH_2 and 170°C , respectively, due to the formation of MgB_2 during dehydrogenation. The reaction of $2\text{LiBH}_4 + \text{MgH}_2 \leftrightarrow 2\text{LiH} + \text{MgB}_2 + 4\text{H}_2$ (11.5 wt. % H_2) was proposed (Figure 2.9).

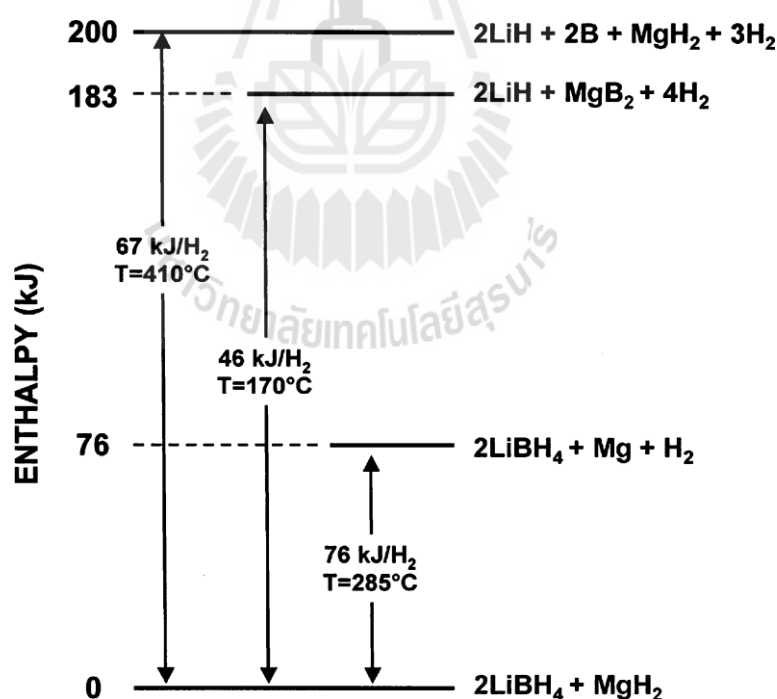
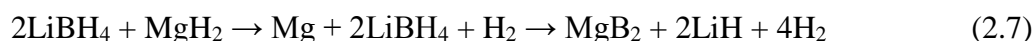


Figure 2.9 Enthalpy diagram for the destabilization of LiBH_4 by MgH_2 (Vajo *et al.*, 2005).

In 2007, Bösenberg *et al.* (Bösenberg *et al.*, 2007) proposed a detailed reaction mechanisms of the $2\text{LiBH}_4\text{-MgH}_2$ composite. The desorption proceeds in two steps as the following the reaction (2.7).



Moreover, the effects of various additives, i.e., titanium isopropoxide (Tiso), vanadium (III) chloride (VCl_3), and silicon oxide (SiO_2), on dehydrogenation of $2\text{LiBH}_4\text{-MgH}_2$ was studied. It was found that Tiso ($2\text{LiBH}_4 + \text{MgH}_2 + 5\% \text{ Tiso}$) showed the positive effect on the sorption kinetics (8.5 wt. % H_2 within 3 h at 300 °C). Moreover, Liu *et al.* (Liu *et al.*, 2013) succeeded in destabilizing LiBH_4 by addition of SrH_2 , via the reaction (2.8) with a theoretical hydrogen capacity of 9.1 wt. %.



Dehydrogenation efficiency of $\text{LiBH}_4/\text{SrH}_2$ system, (Figure 2.10) reveals that pure LiBH_4 releases hydrogen slowly, and the amount of hydrogen desorbed up to 600 °C is only 6.8 wt. %. In contrast, the $\text{LiBH}_4/\text{SrH}_2$ system releases hydrogen in the temperature range of 387-487 °C with a hydrogen capacity of 8.7 wt. %. Therefore, from these results, they found that the thermal stability of LiBH_4 can be remarkable reduced by using SrH_2 as a destabilizing additive. In addition, the dehydrogenation enthalpy and activation energy were decreased from 74 to 48 kJ/mol H_2 and from 111-156 to 64 kJ/mol H_2 , respectively.

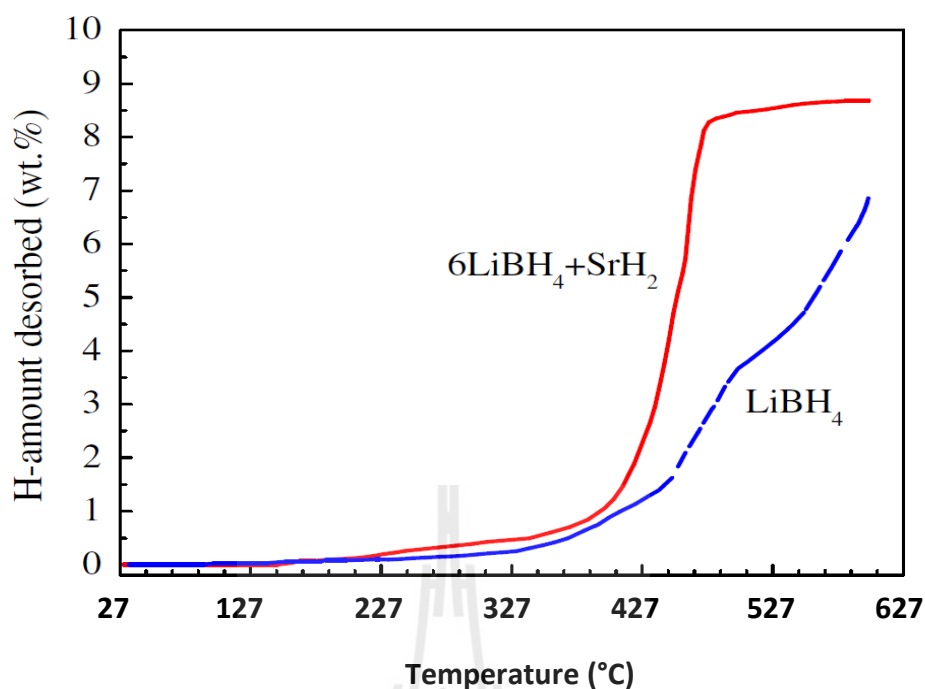


Figure 2.10 Temperature dependence of dehydrogenation for 2 h ball-milled $6\text{LiBH}_4 + \text{SrH}_2$ mixture and pristine LiBH_4 at a heating rate of $2\text{ }^\circ\text{C}/\text{min}$ (Liu *et al.*, 2013).

2.4.3 Nanoconfinement

Furthermore, many research groups focused on the nanoscale effect of metal hydrides, which improves thermodynamic and kinetic properties of hydrogen storage. Nanoconfinement, where the metal hydrides are infiltrated into inert nanoporous network acting as a scaffold for the formation of nanoparticle, is one of the most promising strategies to improve LiBH_4 properties. Via nanoconfinement, several advantages: (i) increased surface area of the reaction, (ii) nanoscale diffusion distances, and (iii) increased number of grain boundaries, which facilitate release and uptake of hydrogen and enhance reaction kinetics are obtained (Nielsen *et al.*, 2010). For example, Gross *et al.* (Gross *et al.*, 2008) infiltrated LiBH_4 into nanoporous carbon scaffold with pore size of 13 nm. They compared the volumetric measurement (a $400\text{ }^\circ\text{C}$ under 1 bar H_2) of dehydrogenation between LiBH_4 in nanoporous carbon

scaffold (pore size of 13 nm) and nonporous graphite (Figure 2.11). They found that, at 5 h, LiBH₄/graphite desorbs only 0.3 wt. % H₂, whereas that of LiBH₄/aerogel is 3.3 wt. %. The total dehydrogenation of LiBH₄/graphite and LiBH₄/aerogel are 2.7 wt. % and 3.7 wt. %, respectively.

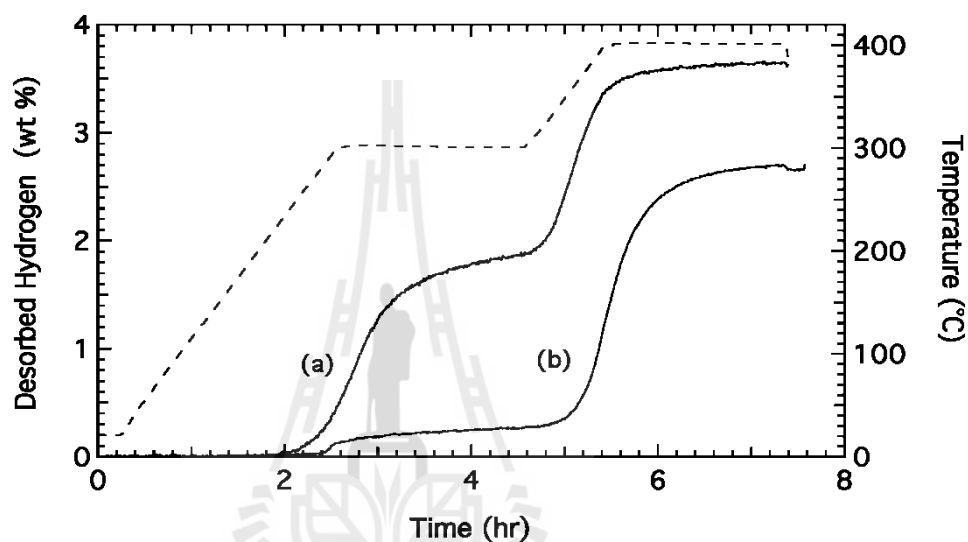


Figure 2.11 Volumetric measurement of dehydrogenation of LiBH₄/aerogel (a) and LiBH₄/graphite (b) (Gross *et al.*, 2008).

Moreover, Liu *et al.* (Liu *et al.*, 2010) synthesized highly ordered nanoporous carbon (NPC) templates with cylindrical pore, (pore size of 2.0 nm) for LiBH₄ nanoconfinement. The hydrogen desorption of LiBH₄ is improved by incorporation into the framework of NPC. The onset desorption temperature of pre-melted LiBH₄ into NPC is significantly reduced from 460 to 220 °C as shown in DSC traces (Figure 2.12). The DSC plots of bulk LiBH₄ and physically mixed LiBH₄/NPC show the phase transition at 115 °C and melting at 284 °C, respectively. The bulk LiBH₄ decomposes at 495 °C and that of physically mixed LiBH₄/NPC is at 350 °C. In the

case of pre-melted $\text{LiBH}_4@\text{NPC}$, DSC result doesn't show any peak of phase transition and melting. This is due to the amorphous state of LiBH_4 nanoconfined in NPC. The main decomposition peak of pre-melted $\text{LiBH}_4@\text{NPC}$ appears at around 339°C , indicating that the decomposition temperature of LiBH_4 is significantly reduced by nanoconfined in NPC.

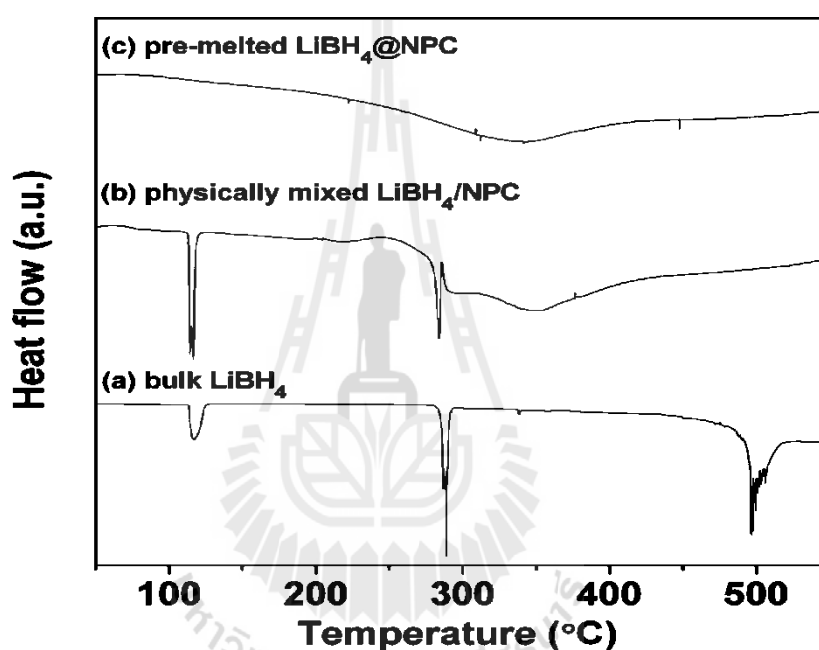


Figure 2.12 DSC traces of (a) bulk LiBH_4 , (b) physically mixed LiBH_4/NPC , and pre-melted $\text{LiBH}_4@\text{NPC}$ (c) (Liu *et al.*, 2010).

Later, the confined LiBH_4 in ordered mesoporous silica (SBA-15) was prepared (Sun *et al.*, 2012) which achieves fast hydrogen release of LiBH_4 at 105°C was achieved. The nanoconfined LiBH_4 in SBA-15 starts to release hydrogen at only 45°C and can release 8.5 wt. % in 10 min (at 105°C under 3-4 bar H_2), and another 2.5 wt. % H_2 in 100 min with slower releasing rate (Figure 2.13). It was ascribed

based on to both the size effect and destabilization of LiBH_4 owing to nanoconfinement and reaction between LiBH_4 and SiO_2 in the $\text{LiBH}_4/\text{SBA-15}$ system.

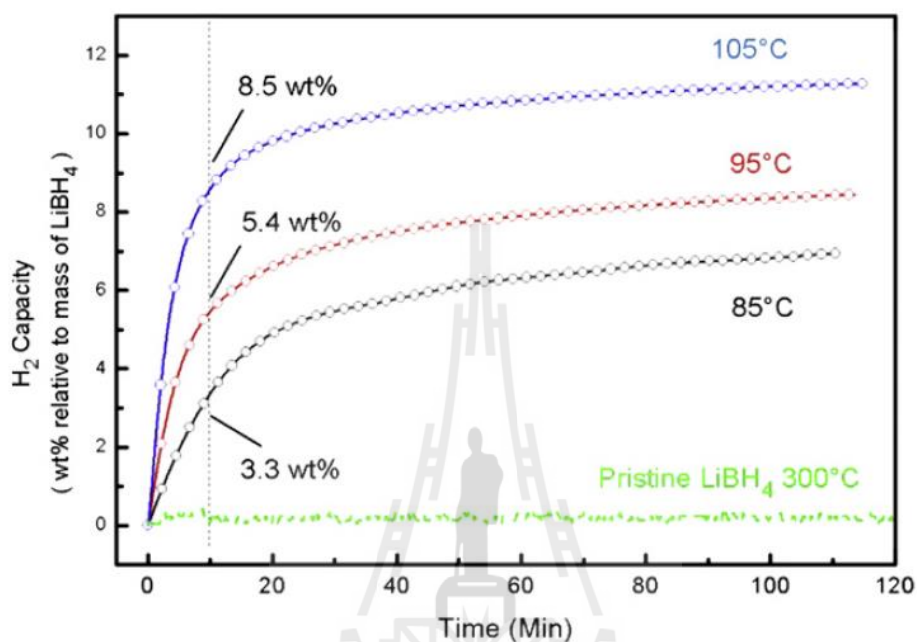


Figure 2.13 Isothermol dehydrogenation curves of $\text{LiBH}_4/\text{SBA-15}$ at 85 °C, 95 °C, and 105 °C. The pristine LiBH_4 hardly decomposed even at 300 °C (Sun *et al.*, 2012).

Later, Nielsen *et al.* (Nielsen *et al.*, 2010) reported a new concept for hydrogen storage of nanoconfined $\text{LiBH}_4\text{-MgH}_2$ composite in nanoporous carbon aerogel scaffold (21 nm pore size). The nanoconfined sample was prepared by solution impregnation of dibutylmagesium (MgBu_2) in heptane solution into carbon aerogel scaffold (CAS) and melt infiltration of LiBH_4 . The hydrogen desorption from nanoconfined $2\text{LiBH}_4\text{-MgH}_2$ and bulk $2\text{LiBH}_4\text{-MgH}_2$ was studied by a simultaneous differential scanning calorimetry, thermogravimetric analysis, and mass spectroscopy (DSC/TGA/MS) (Figure 2.14).

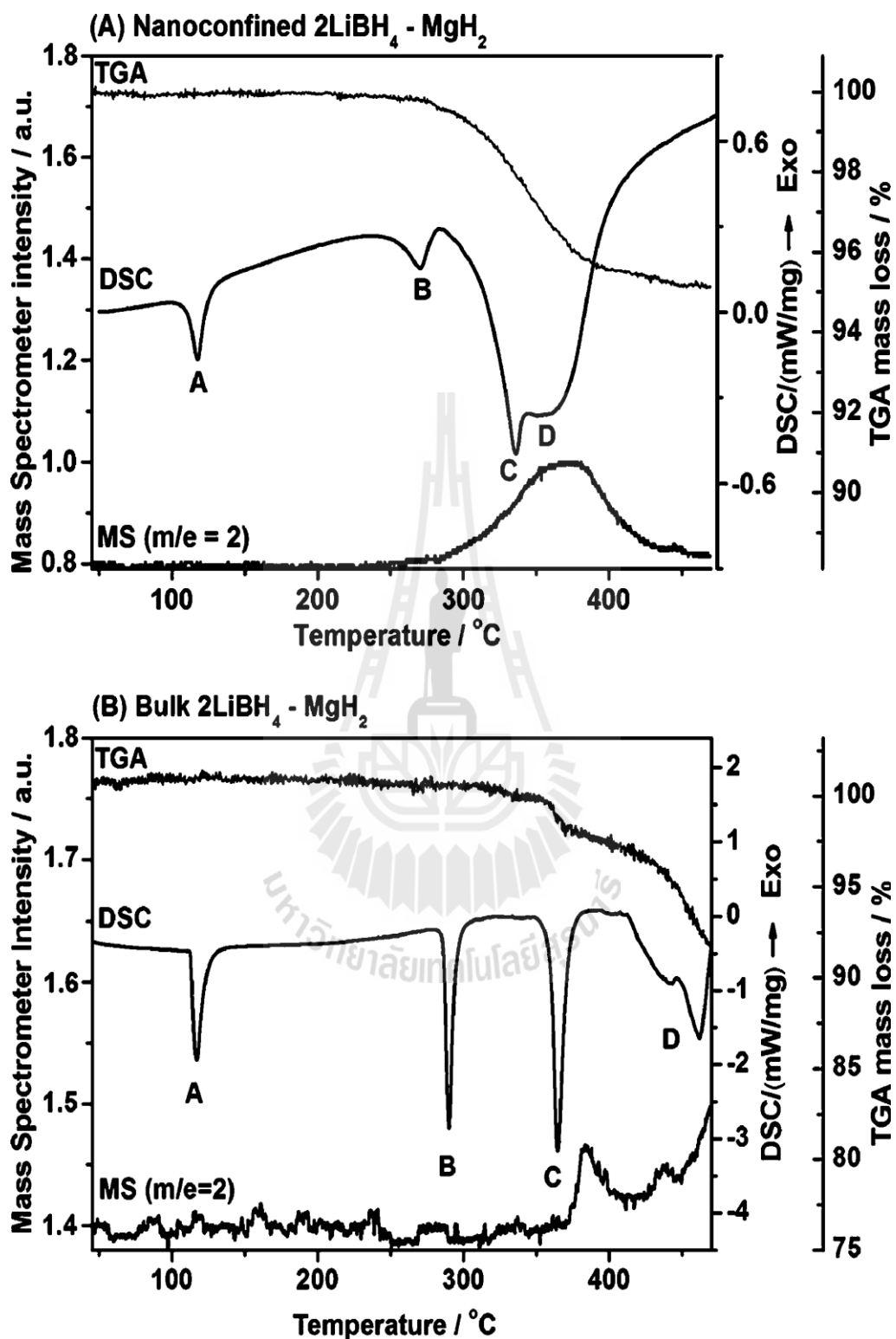


Figure 2.14 Simultaneous DSC-TGA-MS results of nanoconfined $2\text{LiBH}_4\text{-MgH}_2$ (A) and bulk $2\text{LiBH}_4\text{-MgH}_2$ (B) (Nielsen *et al.*, 2010).

The DSC result shows four endothermic desorption peaks denoted A, B, C, and D for both samples, observed at different temperatures. Peak A and B referring to phase transformation and melting point of LiBH_4 , respectively, of nanoconfined and bulk samples are at 113 and 267 °C, and at 117 and 290 °C, respectively. Phase transformation of both samples is observed approximately at the same temperature. The melting point of LiBH_4 shifts significantly to lower temperature after nanoconfinement. Peaks C and D, hinting at dehydrogenation of MgH_2 and LiBH_4 , respectively, of nanoconfined and bulk samples are at 332 and 351 °C, and 364 and 462 °C, respectively. TGA and MS results show that nanoconfined sample release 4.7 wt. % hydrogen in temperature range of 260-470 °C, which is agreement with the calculated mass loss of 4.3 wt % H_2 .

Furthermore, Gosalawit-Utke *et al.* (Gosalawit-Utke *et al.*, 2011) prepared nanoconfined $2\text{LiBH}_4\text{-MgH}_2$ by direct melt infiltration of bulk $2\text{LiBH}_4\text{-MgH}_2$ into nanoporous resorcinol-formaldehyde carbon aerogel scaffold material. The hydrogen desorption kinetics of the nanoconfined $2\text{LiBH}_4\text{-MgH}_2$ is significantly enhanced as compared to bulk $2\text{LiBH}_4\text{-MgH}_2$ (Figure 2.15). Figure 2.15 shows that the hydrogen desorption kinetic rate of nanoconfined $2\text{LiBH}_4\text{-MgH}_2$ is faster as compared to bulk $2\text{LiBH}_4\text{-MgH}_2$. They found that 90% of the total hydrogen content in the nanoconfined $2\text{LiBH}_4\text{-MgH}_2$ released after 1.5 h during the first cycle, while that of bulk $2\text{LiBH}_4\text{-MgH}_2$ is only 34% (at $T=425$ °C and $P(\text{H}_2)=3.4$ bar). Moreover, it also shows superior kinetics of the nanoconfined $2\text{LiBH}_4\text{-MgH}_2$ to the bulk $2\text{LiBH}_4\text{-MgH}_2$ even after four H_2 release and uptake cycles. Moreover, a reversible hydrogen storage capacity of 10.8 wt % H_2 , calculated with respect to the metal hydride content was preserved over all cycles.

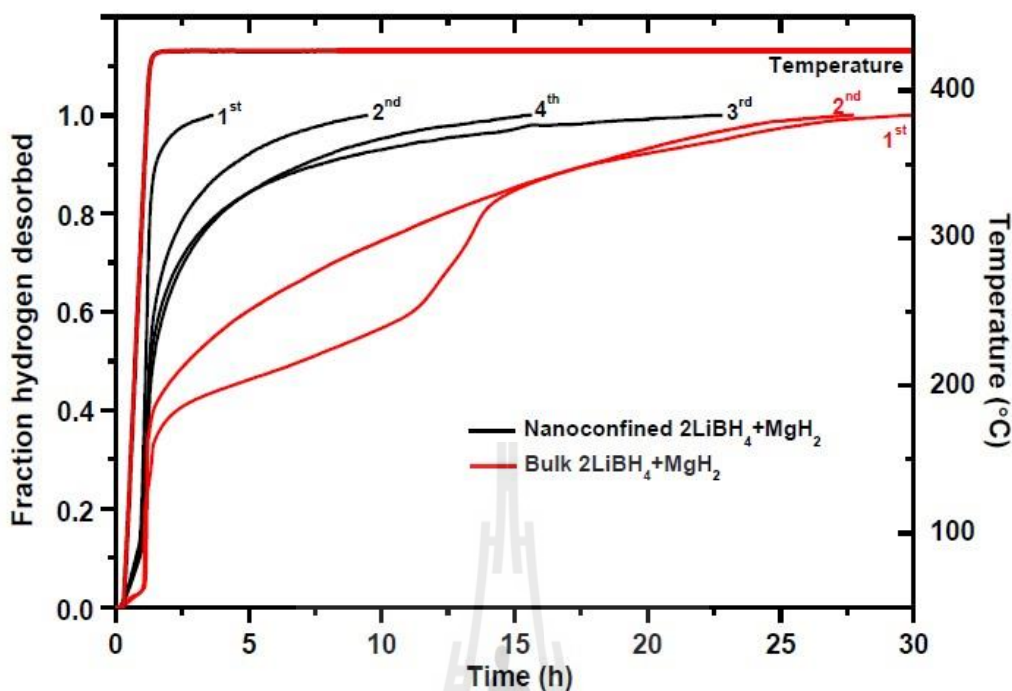


Figure 2.15 Normalized hydrogen desorption profiles of the nanoconfined $2\text{LiBH}_4\text{-MgH}_2$ and bulk $2\text{LiBH}_4\text{-MgH}_2$ (Gosalawit-Utke *et al.*, 2011).

Afterwards, this research group studied and compared the reaction mechanisms, kinetics, and thermodynamics of nanoconfined $2\text{LiBH}_4\text{-MgH}_2$ prepared by two different means of (i) direct melt infiltration (nanoconfined $2\text{LiBH}_4\text{-MgH}_2$) and (ii) solution impregnation of magnesium dibutyl and melt infiltration of LiBH_4 (nanoconfined $2\text{LiBH}_4\text{-MgBu}_2\text{-MgH}_2$) (Gosalawit-Utke *et al.*, 2013). They found that, the kinetics properties of $2\text{LiBH}_4\text{-MgH}_2$ were significant improved after nanoconfinement by both methods. Moreover, the significant reduction in activation energy as compared with the bulk sample (Figure 2.16) is obtained, that is, $\Delta E_A = 132$ and 27 kJ/mol of MgH_2 and LiBH_4 dehydrogenation, respectively, for nanoconfined $2\text{LiBH}_4\text{-MgH}_2$, while those of nanoconfined $2\text{LiBH}_2\text{-MgBu}_2\text{-MgH}_2$ is 86 and 171 kJ/mol, respectively. However, the dehydrogenation enthalpy of MgH_2 and LiBH_4

obtain from both nanoconfined samples are in the range of 41.5-46.2 kJ/mol H₂, which is not significantly different from that of bulk sample (44.13 kJ/mol H₂).

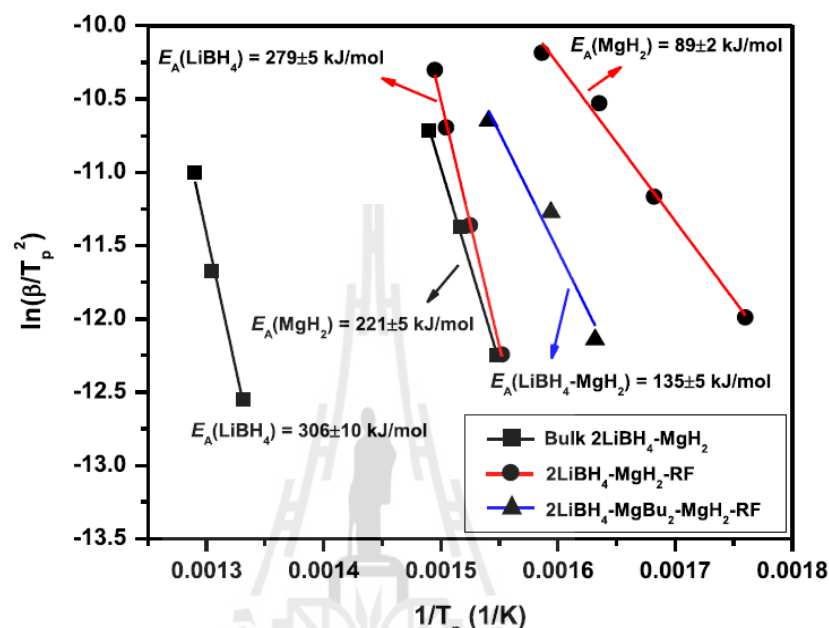


Figure 2.16 Kissinger plots representing the activation energy (E_A) of MgH₂ and LiBH₄ dehydrogenation of bulk and nanoconfined samples (Gosalawit-Utke *et al.*, 2013).

Moreover, they studied the effect of addition of TiCl₃ on nanoconfined 2LiBH₄-MgH₂ for reversible hydrogen storage material (Gosalawit-Utke *et al.*, 2013). The kinetic property improves significantly by adding only 1.6 wt. % TiCl₃ in the nanoconfined 2LiBH₄-MgH₂. For example, nanoconfined 2LiBH₄-MgH₂-TiCl₃ releases total hydrogen within 2 h during the 1st cycle, while nanoconfined and bulk 2LiBH₄-MgH₂ require 4 and 25 h, respectively. The nanoconfined 2LiBH₄-MgH₂-TiCl₃ can reproduce hydrogen after four release and uptake cycles up to 95-98% of the

theoretical hydrogen storage capacity, which is higher than that of nanoconfined $2\text{LiBH}_4\text{-MgH}_2$ in the same temperature and time ranges.

Thus, in the present work, we intend to improve nanoconfinement of both LiBH_4 and MgH_2 by simply method of premilling. MgH_2 is premilled for 5 h to reduce the particle size before milling with LiBH_4 and confining into the nanoporous of carbon aerogel scaffold. The weight ratio of 1:1 (CAS:hydride composite) is used in this work. Base on the melted state of LiBH_4 (at $310\text{ }^\circ\text{C}$), MgH_2 can be transported into the porous structure of CAS. When the particle size of MgH_2 is decreased, the effective nanoconfinement by using LiBH_4 as a carrier should be obtained.

2.5 Research objectives

2.5.1 To nanoconfine 2LiBH_4 -premilled MgH_2 in CAS.

2.5.2 To evaluate the desorption temperature and kinetic efficiency.

2.5.3 To study the reaction mechanisms during melt infiltration, dehydrogenation, and rehydrogenation.

2.5.4 To clarify the effects of MgH_2 premilling on nanoconfinement by comparing with the nanonconfined sample without MgH_2 premilling.

CHAPTER III

EXPERIMENTAL

3.1 Chemicals and materials

The Chemicals and materials used in this work are summarized in Table 3.1

Table 3.1 Chemicals and materials used in this work.

Chemicals /materials	Formula	specification	Supplier
Lithium borohydride	LiBH ₄	90% (hydrogen storage grade)	Sigma-Aldrich
Magnesium hydride	MgH ₂	98% (hydrogen storage grade)	Sigma-Aldrich
Resorcinol	C ₆ H ₆ O	99.0%	Sigma-Aldrich
Formaldehyde	CH ₂ O	37% (in water stabilized by methanol)	QReC
Sodium carbonate	Na ₂ CO ₃	99.999% (anhydrous powder)	Sigma-Aldrich
Acetone	C ₃ H ₆ O	99.8%	Carlo Erbo

3.2 Apparatus

3.2.1 Glove box

Due to the sensitivity of hydride materials to air and moisture, the procedures during sample preparation and some characterizations were handled in an argon atmosphere in the glove box (Omni-Lab System, VAC).



Figure 3.1 A glove box used in the laboratory.

3.2.2 Ball mill

A Spex 8000 M Mixer/Mill was used for reducing the particle size of powder sample.

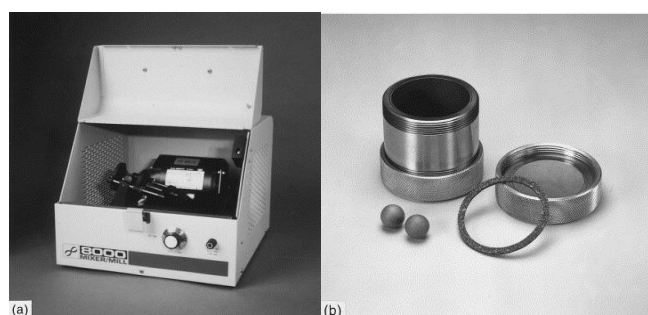


Figure 3.2 A Spex 8000 M Mixer/Mill (a) and tungsten carbide vial set (b).

3.3 Instruments

3.3.1 N₂ adsorption-desorption, (Nova 2200e from Quantachrome) was used to investigate the surface area, pore size, and total pore volume.

3.3.2 Scanning electron microscopy (SEM), (Auriga, a Zeiss), energy dispersive X-ray spectroscopy (EDS), and elemental mapping, (EDAX Inc., UAS) were used for morphological studies and elemental analyses.

3.3.3 Simultaneous Thermal Analysis (STA), (449 F3, a Netzsch) and Mass Spectroscopy (MS), was used for investigation of dehydrogenation process.

3.3.4 In situ synchrotron radiation powder X-ray diffraction (SR-PXD), (at MAX II Synchrotron, beamline I711 in the research laboratory of MAX-Lab, Lund, Sweden) was used to investigate the phases during dehydrogenation.

3.3.5 Fourier Transform Infrared Spectrometry (FTIR), (T27/Hyp 2000, a Bruker) was used to investigate the function groups in the sample.

3.3.6 Nuclear magnetic resonance (NMR), (ASCEND™ 500, a Bruker) was used to investigate the chemical environment of hydrogen storage materials and chemisorbed hydrogen atom.

3.3.7 Sievert-type apparatus, (Laboratory scale test station) was used to measure the hydrogen desorption/absorption, and cycling efficiency.

3.4 Sample preparation

3.4.1 Synthesis of carbon aerogel scaffold

The resorcinol formaldehyde aerogels were prepared according to previously published procedures (Gosalawit *et al.*, 2011; Al-Muhtaseb *et al.*, 2003; Xu *et al.*, 2012; and Tao *et al.*, 2008). The carbon aerogels were synthesized by

mixing 20.700 g of resorcinol, 11.29 g of a 37 wt. % formaldehyde, 0.0969 g, and 33.84 g of deionized water and sodium carbonate in a beaker with continuous stirring. The mixture was stirred until a homogeneous solution was obtained. Once prepared, solutions were transferred to 250 mL glass bottles, sealed, and aged for 24 h at room temperature, for 24 h at 50 °C, and for 72 h at 90 °C. The gels were cooled to room temperature, cut into cubes (1 cm³), and immersed in acetone bath. The acetone bath was changed twice within a period of 24 h. The aerogel cubes were dry in air for several days. The dried gels were pyrolyzed by heating to 800 °C (2.6 °C/min) under nitrogen atmosphere in a tube oven, dwelling at 800 °C for 6 h, and cooling to room temperature.

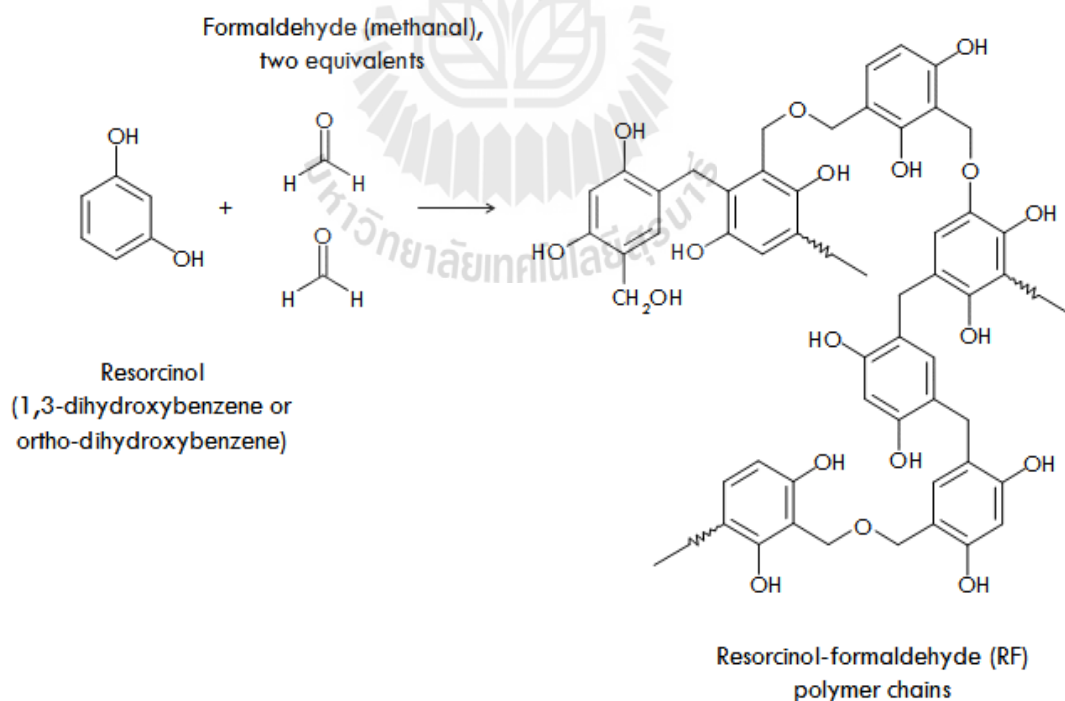


Figure 3.3 Reaction mechanisms during cross-linked polymerization (<http://www.aerogel.org/?p=71>).

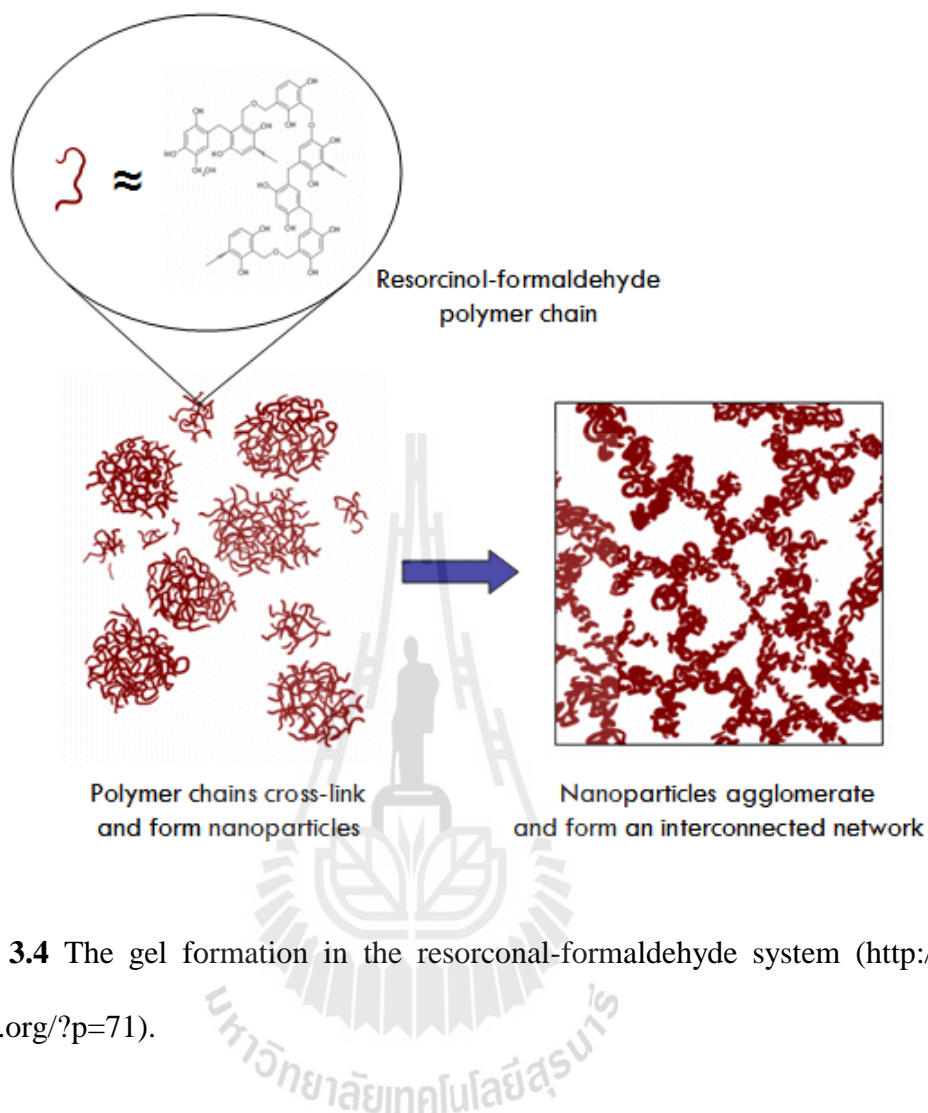


Figure 3.4 The gel formation in the resorcinol-formaldehyde system (<http://www.aerogel.org/?p=71>).

3.4.2 Ball milling of metal hydrides

The powder of MgH_2 was pre-milled in stainless steel vial by using a SPEX CertiPrep 8000 D Dual MIXER/MILL for 5 h to obtain premilled MgH_2 . The ball-to-powder weight ratio (BPR) and milling speed are of 10:1 and 1725 rpm, respectively. The fresh and premilled MgH_2 was milled with LiBH_4 in the molar ratio of 1:2 ($\text{MgH}_2\text{-LiBH}_4$) by using the same milling condition as premilled MgH_2 to obtain $2\text{LiBH}_4\text{-MgH}_2$ and $2\text{LiBH}_4\text{-premilled MgH}_2$. The milled samples of $2\text{LiBH}_4\text{-premilled MgH}_2$ and $2\text{LiBH}_4\text{-MgH}_2$ were mixed CAS at weight ratio of 1:1 in the

mortar denoted as mixed CAS-2LiBH₄-premilled MgH₂ and CAS-2LiBH₄-MgH₂, respectively.

3.4.3 Melt infiltration

To melt infiltrate 2LiBH₄-MgH₂ and 2LiBH₄-premilled MgH₂ into the nanopore of carbon aerogel scaffold, the powder sample of mortar-mixed CAS-2LiBH₄-MgH₂ and CAS-2LiBH₄-premilled MgH₂ were heated to 310 °C under 60 bar H₂, dwelling at 310 °C for 1 h, and cooling to room temperature.

3.5 Sample characterizations

3.5.1 N₂ adsorption-desorption

Nanoconfined samples and CAS were characterized by N₂ absorption-desorption technique. The CAS was degassed at 200 °C under vacuum for several h, before the measurement. The specific surface area of the sample was calculated following the Brunner Emmet Teller (BET) method and the Barrett Joyner Halenda (BJH) method at the relative pressure range 0-1 (p/p_0) of liquid nitrogen and the total volume was calculated from a single point at $p/p_0 \sim 1$. Data were analyzed using the Brunner-Emmett-Teller (BET), Barrett-Joyner-Halenda (BJH), and t-plot methods.

3.5.2 Scanning Electron Microscopy (SEM), Energy Dispersive X-ray Spectroscopy (EDS), and elemental mapping

SEM-EDS-mapping technique was used for morphological studies and elemental analysis. The powder sample was deposited onto the sample holder by using silver glue. The sample was coated by palladium-gold sputtering with the current of 30 mA for 30 s under vacuum. An internal view of the specimen was

prepared by a focused ion beam technique (FIB) using a Canixon from Orsay Physics, France. The specimen was shot by gallium ion beam with the energy of 30 kV.

3.5.3 Simultaneous Thermal Analysis (STA) and Mass Spectroscopy (MS)

Differential scanning calorimetry (DSC) and thermogravimetric analysis (TG) were carried out by heating the sample from room temperature to 500 °C with a heating rate of 5 °C/min under the nitrogen flow of 50 mL/min. The relative composition of hydrogen in the exhaust gas was continuously investigated by a mass spectrometry (MS). During the experiment, the MS signals at $m/e = 2$ was recorded in order to detect H₂. Up to 10-15 mg of powdered sample was placed in a alumina crucible. The samples were prepared in the argon-filled glove box to protect the oxygen contamination.

3.3.4 In situ Synchrotron Radiation powder X-ray Diffraction (SR-PXD)

The in situ SR-PXD was detected by a MAR165 CCD detector with the selected X-ray wavelength of 0.988762 Å. The powder samples were refilled airtight in sapphire capillaries in a purified argon atmosphere in the glove box. Heating was applied by a tungsten wire placed under the capillary, whereas the temperature was controlled by an external PID regular and thermocouple inserted into the powder-bed as shown elsewhere. On the basis of a temperature control, a deviation between the real and measured temperatures was observed at elevated temperatures. The dehydrogenation was investigated by heating the melt infiltrated powder sample from room temperature to 350 °C (5 °C/min) under 3-4 bar H₂, dwelling at 350 °C for 30 min, and cooling to room temperature.

3.5.5 Fourier Transform Infrared Spectrometry (FTIR)

Fourier Transform Infrared Spectrometry (FTIR) was carried out in the

wavenumber rang of 400-4000 cm^{-1} and the number of scans was 64. The KBr power is dried at 120 °C overnight. The sample powder is mixed with dried KBr and ground with a mortar. The mixture of sample and KBr was pressed under specific pressure to obtain KBr pellet. The KBr pellet containing the sample was assembled a FTIR spectrometer.

5.5.6 Nuclear Magnetic Resonance (NMR) measurement

^1H and ^{11}B nuclear magnetic resonance (NMR) spectra were recorded by a Bruker ASCEND™ 500 spectrometer using a BL4 VTN probe for 4 mm outer diameter rotors. The NMR measurements were performed at 25 °C and the samples were tightly packed in a zirconia end-capped tube in the glove box. A spinning speed of 10 kHz was used together with 2000 and 50 scans for ^{11}B and ^1H NMR, respectively. The excitation pulse lengths of ^{11}B and ^1H were 5.0 and 4.0 μs , respectively. The relaxation delay was 5.0 s for both ^{11}B and ^1H NMR, while that of MgH_2 (^1H MAS NMR) was 20.0 s. The scanning width of ^{11}B NMR for LiBH_4 was 250 to -250 ppm, whereas those of ^1H MAS NMR were 100 to -100 and 18 to -2 ppm for LiBH_4 and MgH_2 , respectively. The ^{11}B and ^1H chemical shifts were detected in part per million (ppm) relative to neat boric acid (H_2BO_3) and tetramethylsilane ($\text{Si}(\text{CH}_3)_4$), respectively.

5.5.7 Sievert-Type Apparatus

The hydrogen dehydrogenation/rehydrogenation properties of the samples were measured by a Sievert-type apparatus, assembled in the Chemistry Laboratory (F2) as shown in Figures 3.5 and 3.6. A sample of about 50-80 mg was packed to the sample holder, which done in the glove box under an argon atmosphere. Afterwards, the sample was installed to Sievert-type apparatus. The dehydrogenation

was investigated by heating the powder sample to 320 °C under 4-5 bar H₂. Rehydrogenation was carried out at 320 °C under 80 bar H₂ for 12 h. The amount of hydrogen release and uptake was calculated by the pressure change (ΔP) using the following equations:

$$(\Delta P)V = nRT \quad (3.1)$$

$$\text{H}_2 \text{ desorbed (wt. \%)} = [(n \times 2.0158)/\text{sample weight}] \times 100$$

where P, V, and T are H₂ pressure (atm), volume of the system (L), and temperature (K), respectively, n is the number of hydrogen moles (mol), and R is gas constant (0.0821 L atm K⁻¹ mol⁻¹).



Figure 3.5 Sievert-type apparatus assembled in the Chemistry Laboratory (F2).

CHAPTER IV

RESULTS AND DISCUSSION

4.1 Melt infiltration

To confirm successful nanoconfinement of 2LiBH₄-premilled MgH₂ composite into CAS, N₂ adsorption-desorption experiment were carried out. From Table 4.1, CAS shows a specific surface areas (S_{BET}), a pore size (D_{max}), and a total pore volume (V_{tot}) of 575 m²/g, 8.73 nm, and 0.71 cm³/g, respectively. After melt infiltration of milled 2LiBH₄-MgH₂, the surface area and the total pore volume reduce to 102 m²/g and 0.22 cm³/g, respectively. This indicates successful nanoconfinement of metal hydride composite in CAS as similar as previous report (Gosalawit-Utke *et al.*, 2011). In the case of nanoconfined 2LiBH₄-premilled MgH₂, the surface area and total pore volume reduce to 15 m²/g and 0.06 cm³/g, respectively, (Table 4.1). From these results, it should be noted that effective nanoconfinement of complex hydride is obtained by MgH₂ premilling.

Table 4.1 Texture parameter of CAS, nanoconfined 2LiBH₄-MgH₂, and nanoconfined 2LiBH₄-premilled MgH₂.

samples	S_{BET}	V_{micro}	V_{meso}	D_{max}	V_{tot}
	(m²/g)	(cm³/g)	(cm³/g)	(nm)	(cm³/g)
CAS	575	0.12	0.58	8.73	0.71
Nanoconfined 2LiBH ₄ -MgH ₂	102	0	0.22	8.66	0.22
Nanoconfined 2LiBH ₄ -premilled MgH ₂	15	0	0.08	5.98	0.06

To further confirm the effective nanoconfinement, the SEM-EDS-mapping technique was used to analyze the elemental compositions inside CAS. By using focus ion beam (FIB) technique, the monoliths of nanoconfined 2LiBH₄-MgH₂ and 2LiBH₄-premilled MgH₂ were irradiated by gallium (Ga) ion beam, to get the view inside of the sample (Figure 4.1 (A) and (B), respectively). Positions (×) and (+) in the SEM images of nanoconfined 2LiBH₄-MgH₂ and 2LiBH₄-premilled MgH₂, referring to surface and internal area of the sample bulk, respectively, are respected for elemental analyses as shown in Figures 4.1 (C), (D), (E), and (F). From Figures 4.1 (C) and (E) referring to Figure 4.1 (A) at the positions of (×) and (+), respectively, they give the signals of carbon (C) from CAS, Oxygen (O), gallium (Ga), and platinum (Pt) from oxidation in air and FIB technique, respectively. In the case of Mg and B from LiBH₄ and MgH₂, respectively, they are found on the surface and inside the sample (Figures 4.1 (C) and (E)). For nanoconfined 2LiBH₄-premilled MgH₂, all elements detected are similar to those of nanoconfined sample without MgH₂ premilling (Figures 4.1 (D) and (F)).

obtained from Figure 4.1 (B) at position (×) and (+), respectively). Figure 4.1 (D) reveals the signals of Mg and B on the surface of the sample bulk. Moreover, the signal of Mg is also observed inside the porous structure of CAS together with slight signal of B (Figure 4.1 (F)). It should be noted that the amount of Mg nanoconfined in CAS structure is due to MgH₂ premilling.

Furthermore, the nanoconfined 2LiBH₄-MgH₂ and 2LiBH₄-premilled MgH₂ were investigated by elemental-mapping to study the elemental distribution inside the sample. SEM images (Figures 4.2 and 4.3 (A)) and elemental-mapping of carbon (C), boron (B), and magnesium (Mg) (Figures 4.2 and 4.3 (B), (C), and (D)), respectively, of nanoconfined 2LiBH₄-MgH₂ and 2LiBH₄-premilled MgH₂ are studied. From B-mapping of nanoconfined sample without MgH₂ premilling (Figure 4.2 (C)), it shows good distribution of B from LiBH₄ both inside and outside the bulk sample. In the case of Mg-mapping (Figure 4.2 (D)), a lot of Mg particles are outside the pore of CAS but they also show good distribution of Mg at the yellow spots in the CAS structure. Hence, this confirms nanoconfined MgH₂ inside the CAS. For nanoconfined 2LiBH₄-premilled MgH₂, B-mapping shows also good distribution as same as the B-mapping of nanoconfined 2LiBH₄-MgH₂ (Figure 4.3 (C)). In the case of Mg-mapping, a lot of Mg particles are inside the pore of CAS together with slight agglomeration on the surface of CAS (Figure 4.3 (D)). Thereby, MgH₂ with premilling is significantly nanoconfined in CAS more than that of MgH₂ without premilling as shown as several bright yellow areas inside the pore of CAS (Figure 4.3 (D)). The results show that effective nanoconfinement of both LiBH₄ and MgH₂ can be improved by MgH₂ premilling before direct melt infiltration. This could be due to the fact that the particle size of MgH₂ was reduced by ball milling.

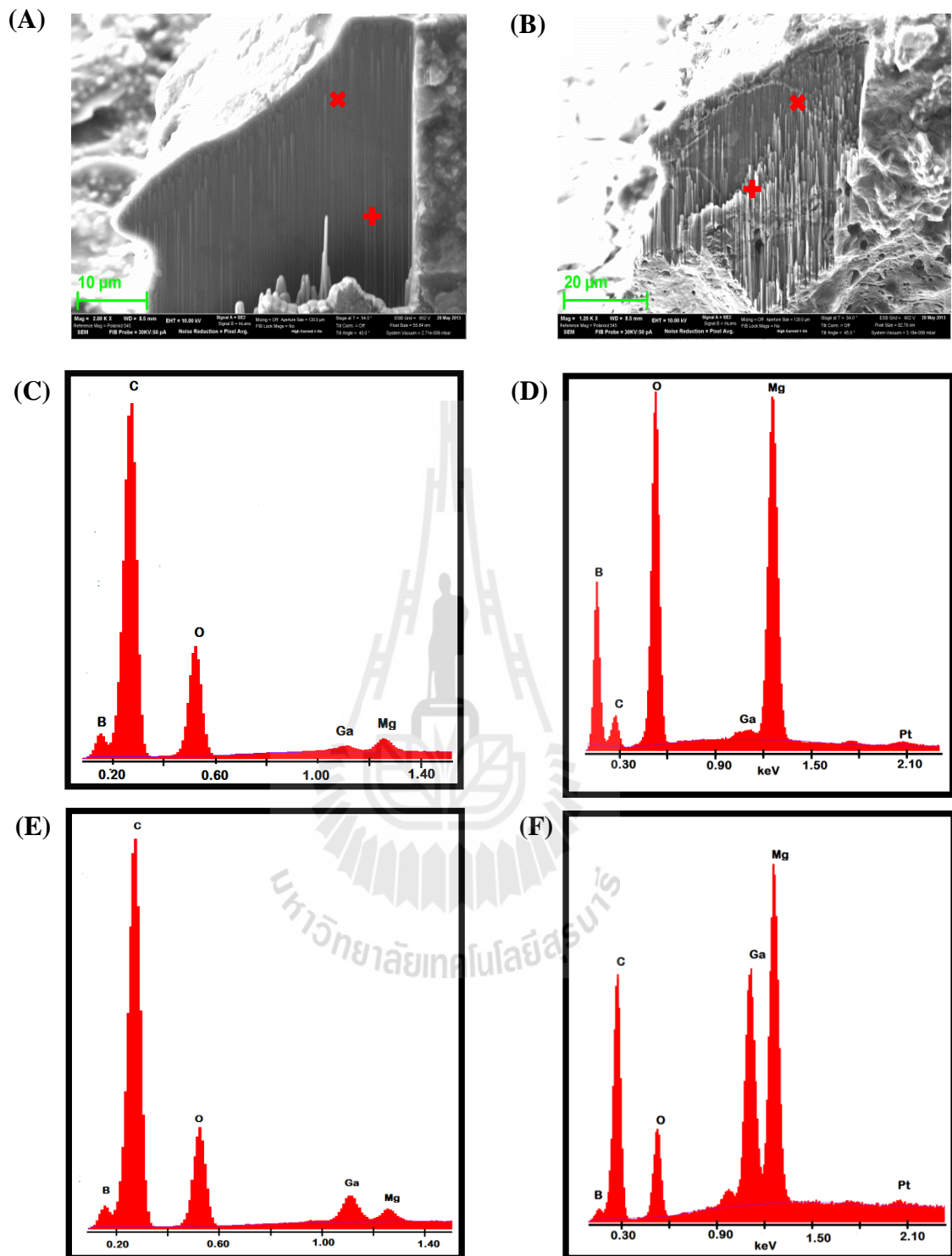


Figure 4.1 SEM images and elemental analysis (EDS results) on the surface (×) and inside the sample bulk (+) of nanoconfined 2LiBH₄-MgH₂ (A, C, and E) and nanoconfined 2LiBH₄-premilled MgH₂ (B, D, and F).

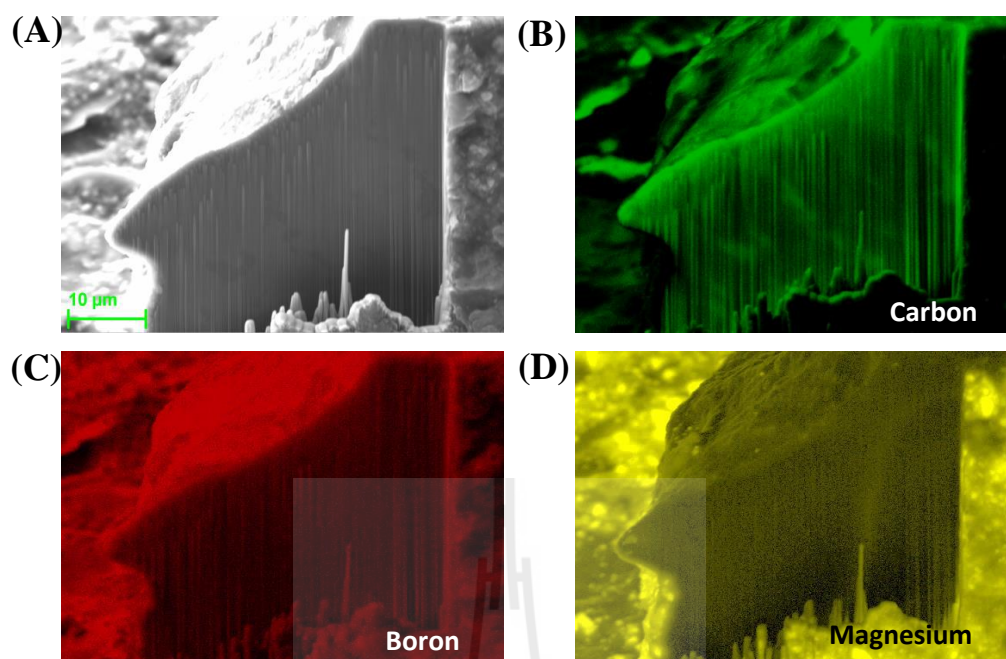


Figure 4.2 SEM micrograph of nanoconfined $2\text{LiBH}_4\text{-MgH}_2$ (A), carbon mapping mode (B), boron mapping mode (C), and magnesium mapping mode (D).

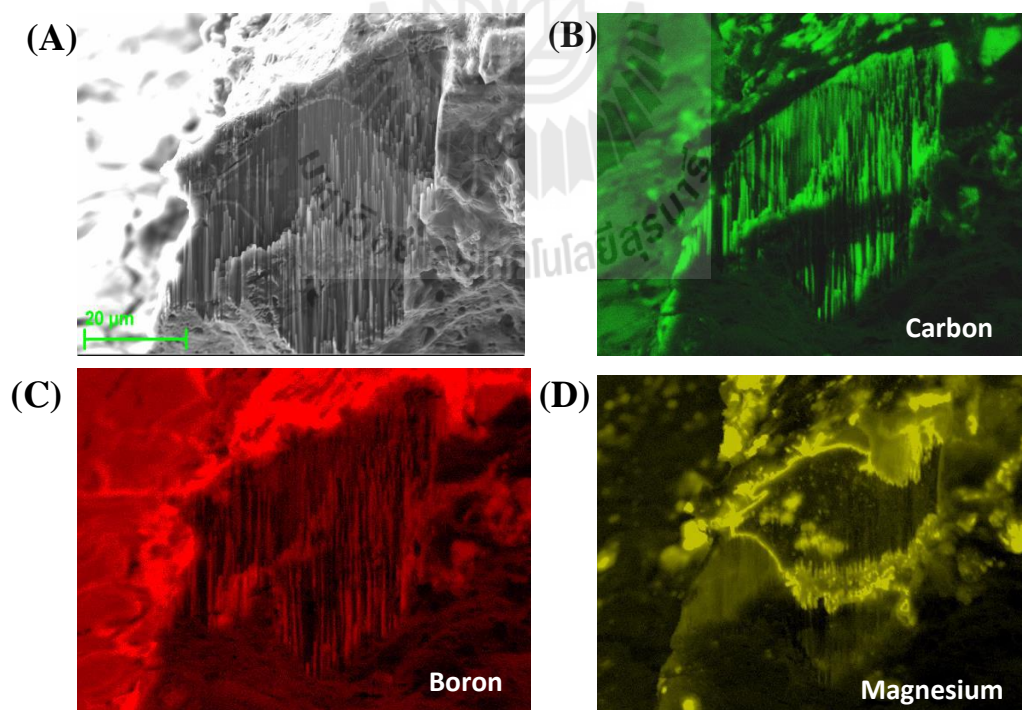


Figure 4.3 SEM micrograph of nanoconfined $2\text{LiBH}_4\text{-premilled MgH}_2$ (A), carbon mapping mode (B), boron mapping mode (C), and magnesium mapping mode (D).

4.2 Dehydrogenation and reaction mechanisms

The hydrogen dehydrogenation of nanoconfined 2LiBH₄-premilled MgH₂ and 2LiBH₄-MgH₂ were performed by simultaneous thermal analysis (STA) and mass spectroscopy (MS). In Figure 4.4 (A), the DSC themogram shows five endothermic peaks of nanoconfined 2LiBH₄-MgH₂. The peaks at 107 and 254 °C refer to phase transformations of α-β LiBH₄ and the melting of LiBH₄, respectively. Afterwards, three steps of dehydrogenation at 348, 389, and 430 °C referred to the dehydrogenation of MgH₂ and LiBH₄, respectively, are observed. The TGA result shows the hydrogen mass loss of 3.9 wt. %. The hydrogen content of bulk 2LiBH₄-MgH₂ composite is 11.4 wt. % according to equation 4.1 (Vajo *et al.*, 2005).



Therefore, with respect to the weight ratio of 2LiBH₄-MgH₂:CAS (1:1 weight ratio), theoretical hydrogen content of 5.7 wt. % H₂ is obtained. The MS result shows that the dehydrogenation starts very quickly at the temperature about 200 °C and finishes at the temperature higher than 450 °C. In addition, diborane (B₂H₆) gas is also released during dehydrogenation. Thus, 3.9 wt. % H₂ released from nanoconfined 2LiBH₄-MgH₂ not only belong to hydrogen but also B₂H₆ (MS result in Figure 4.4 (A)). For the nanoconfined 2LiBH₄-premilled MgH₂, the DSC result (Figure 4.4 (B)) shows that the phase transformation and the melting point of LiBH₄ are observed at 109 and 255 °C, respectively. This is in agreement with the nanoconfined sample without MgH₂ premilling. The dehydrogenation of MgH₂ and LiBH₄ is obtained at 345 °C which is corresponding to the MS result. MS results show only hydrogen released in the temperature range of 320-400 °C, while that of B₂H₆ is not detected. From TGA themogram, thus, it shows only single step of dehydrogenation with 4.2

wt. % hydrogen. These results indicate that the nanostructure alters the dehydrogenation pathway and eliminates the formation of B_2H_6 (Lui *et al.*, 2010).

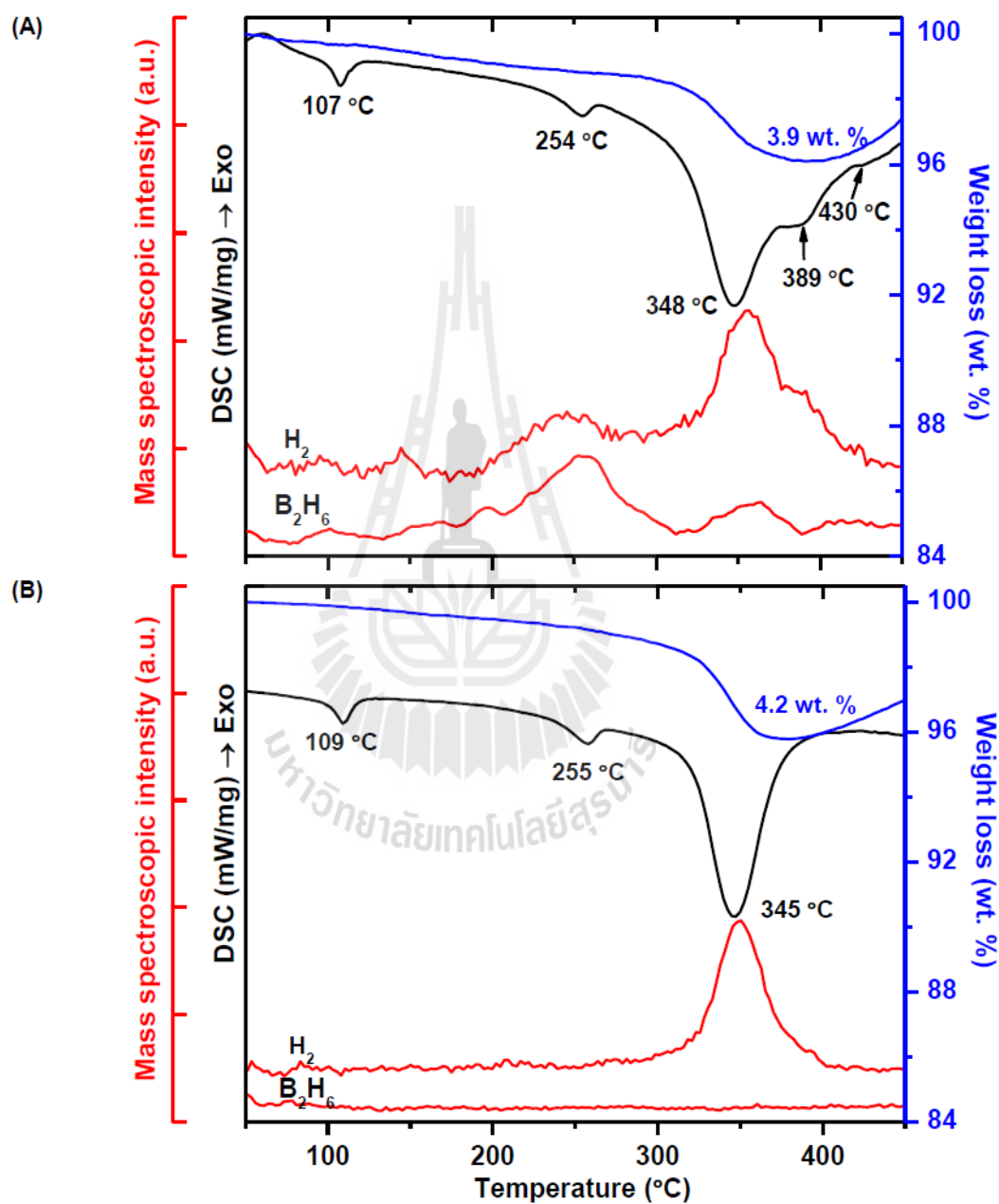


Figure 4.4 Simultaneously performed DSC-TGA-MS of the hydrogen release reactions from the nanoconfined 2LiBH₄-MgH₂ (A) and the nanoconfined 2LiBH₄-premilled MgH₂ (B).

To clarify the processes during the melt infiltration of nanoconfined $2\text{LiBH}_4\text{-MgH}_2$ and nanoconfined $2\text{LiBH}_4\text{-premilled MgH}_2$ based on N_2 adsorption-desorption, SEM-EDS-mapping, and simultaneous DSC-TGA-MS results, the schematic draw as in Figure 4.5 is proposed. Regarding the melt infiltration at melting point of LiBH_4 (at $310\text{ }^\circ\text{C}$), the small particles of MgH_2 are transferred into the porous structure of CAS by liquid LiBH_4 whereas the big MgH_2 particles cannot be confined and thus blocked the pore of CAS. As a consequence, this leads to limited amount of LiBH_4 nanoconfined and results in the dehydrogenation at higher temperature and release of B_2H_6 . The elemental mapping of Mg (Figure 4.2(D)) exhibits less particles of Mg dispersed inside CAS for nanoconfined $2\text{LiBH}_4\text{-MgH}_2$ as compared with that in nanoconfined sample with MgH_2 premilling (Figure 4.3(D)). In the case of nanoconfined $2\text{LiBH}_4\text{-premilled MgH}_2$ (Figure 4.5 (B)), the particles of MgH_2 were reduced by high energy ball milling, thus, the nanoparticles of MgH_2 can be transported to the pore of CAS easier than that of nanoconfined $2\text{LiBH}_4\text{-MgH}_2$. As a result, the effective nanoconfinement of both LiBH_4 and MgH_2 can be accomplished by simply method of MgH_2 premilling.

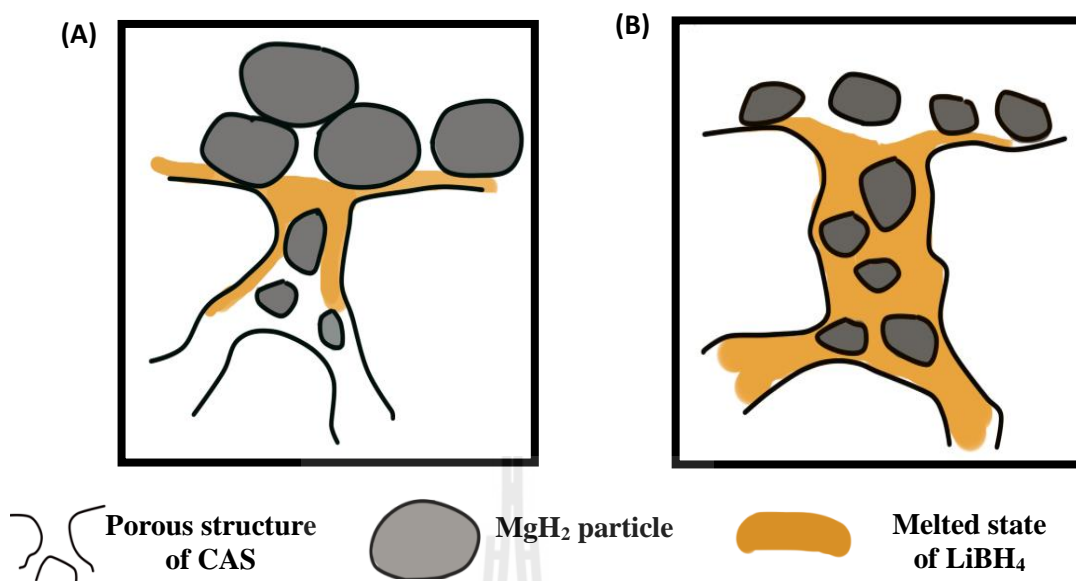


Figure 4.5 Schematic draw of the process for nanoconfined 2LiBH₄-MgH₂ (A) and nanoconfined 2LiBH₄-premilled MgH₂ (B).

Furthermore, the reaction mechanisms during dehydrogenation were studied by in situ SR-PXD measurement (Figure 4.6). The sample was heated from room temperature to 350 °C (heating rate 5 °C/min) under hydrogen pressure of 3-4 bar and dwelled at 350 °C for 30 min. The diffraction peaks of α -LiBH₄, MgH₂, MgO, and MgB₂ are detected at the room temperature. The formation of MgB₂ refers to the dehydrogenation and the reaction of LiBH₄ and MgH₄ during the melt infiltration as same as the previous work of nanoconfined 2LiBH₄-MgH₂ (2:1 weight ratio of CAS:hydride composite) (Gosalawit-Utke *et al.*, 2011). Afterward, the phase transformation (from *o*-LiBH₄ to *h*-LiBH₄) and melting of *h*-LiBH₄ are appeared at ~82 °C and 146 °C, respectively. The results are not corresponded to the DSC result (Figure 4.4 (B)) because only a small amount of the sample packed in the capillary was used for the in situ SR-PXD measurement. The diffraction peaks of MgH₂

disappear at 270 °C, corresponding to the formation of Mg and the enhancement of MgB₂. With respect to the previous work of nanoconfined 2LiBH₄-MgH₂ (2:1 weight ratio of CAS:hydride composite) (Gosalawit-Utke *et. al.*, 2011), the dehydrogenation of MgH₂, which produces Mg, is observed at 336 °C and Mg reacts with LiBH₄ to form MgB₂ at 390 °C. Moreover, the rest of MgH₂ stay as a metallic Mg upon the dehydrogenation. From this work, the dehydrogenation of MgH₂ and the formation of MgB₂ are found at low temperature of 270 °C. Thereafter, the diffraction peaks of Mg disappear, whereas those of MgO and MgB₂ slightly increase at 339 °C, suggesting further reaction of Mg with oxygen and LiBH₄, respectively. After the isothermal at 350 °C for 30 min and cooling to room temperature, MgO and MgB₂ are observed. This indicates that the complete dehydrogenation of MgH₂ to produce Mg, which further react with LiBH₄ to produce MgB₂, are obtained as previously reported (Gosalawit-Utke *et. al.*, 2011). The diffraction peaks of MgO are found at all temperatures during dehydrogenation and it increases after MgH₂ dehydrogenation, corresponding to the reaction between MgH₂ and some oxygen during the experiment. Moreover, at the temperature range of 96-135 and 189-350 °C there are the formations of unknown intermediate phases.

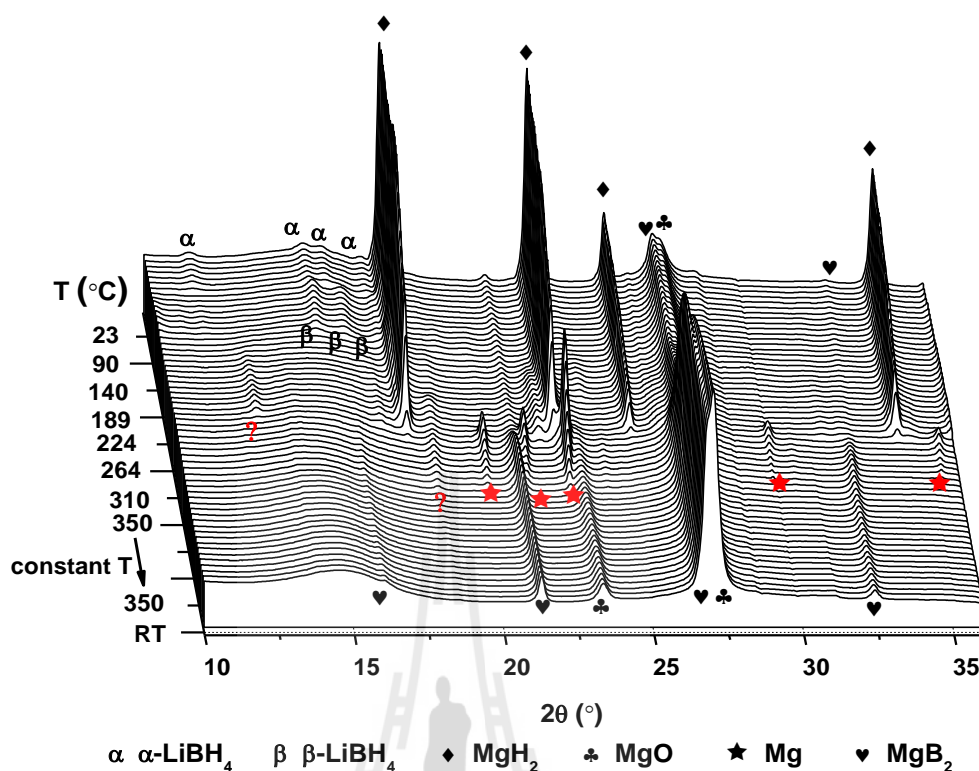


Figure 4.6 SR-PXD spectra of the nanoconfined 2LiBH₄-premilled MgH₂ during dehydrogenation.

To confirm the reversibility of nanoconfined 2LiBH₄-pre-milled MgH₂, the FT-IR experiment was studied as shown in Figure 4.7. From Figure 4.7 (a), nanoconfined 2LiBH₄-premilled MgH₂ shows B-H vibration of stretching (2224, 2299, and 2389 cm⁻¹) and bending (1127 cm⁻¹) (Crosby *et al.*, 2010), which confirm the existence of LiBH₄ nanoconfined in CAS. The peak at 1634 cm⁻¹ refers to a O-H bond, which comes from oxidation in air and moisture during experiments. The sample after dehydrogenation (Figure 4.7 (b)) reveals the FT-IR spectra of B-H bending and B-H stretching modes with lower intensity, indicating dehydrogenation of LiBH₄. For the sample after rehydrogenation (Figure 4.7 (c)), the FT-IR spectrum shows the peaks of all B-H vibration modes of LiBH₄, confirming reversibility of

LiBH₄ in nanoconfined 2LiBH₄-premilled MgH₂. Furthermore, the stable phase of [B₁₂H₁₂]²⁻ found generally at 2480 cm⁻¹ (Gosalawit-Utke *et al.*, 2013) is luckily not found in FTIR spectrum of nanoconfined 2LiBH₄-premilled MgH₂ after rehydrogenation.

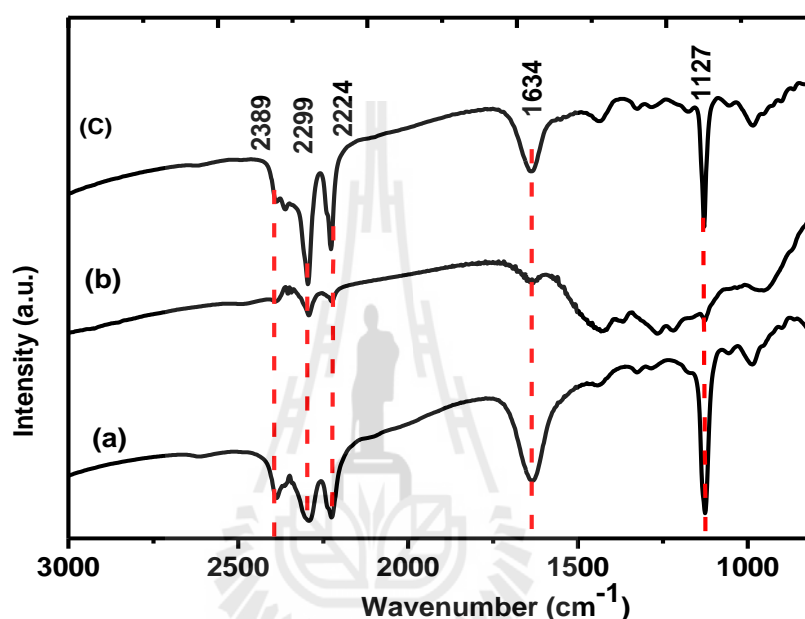


Figure 4.7 FT-IR spectra of nanoconfined 2LiBH₄-premilled MgH₂ before dehydrogenation (a), after dehydrogenation (b), and after rehydrogenation (c).

Furthermore, the reversibility of MgH₂ was confirmed by the ¹H MAS NMR experiments. Figures 4.8 (A) and (B) show the ¹H NMR of pure LiBH₄ and pure MgH₂ at 2.8 and 8.0 ppm (Buht *et al.*, 2009; Corey *et al.*, 2008; Shane *et al.*, 2010; Niraj *et al.*, 2012; and Grzech *et al.*, 2012), respectively. In the case of nanoconfined 2LiBH₄-premilled MgH₂ after rehydrogenation, it reveals the characteristic ¹H MAS NMR peaks of both LiBH₄ and MgH₂. This confirms successful reversibility of nanoconfined 2LiBH₄-premilled MgH₂.

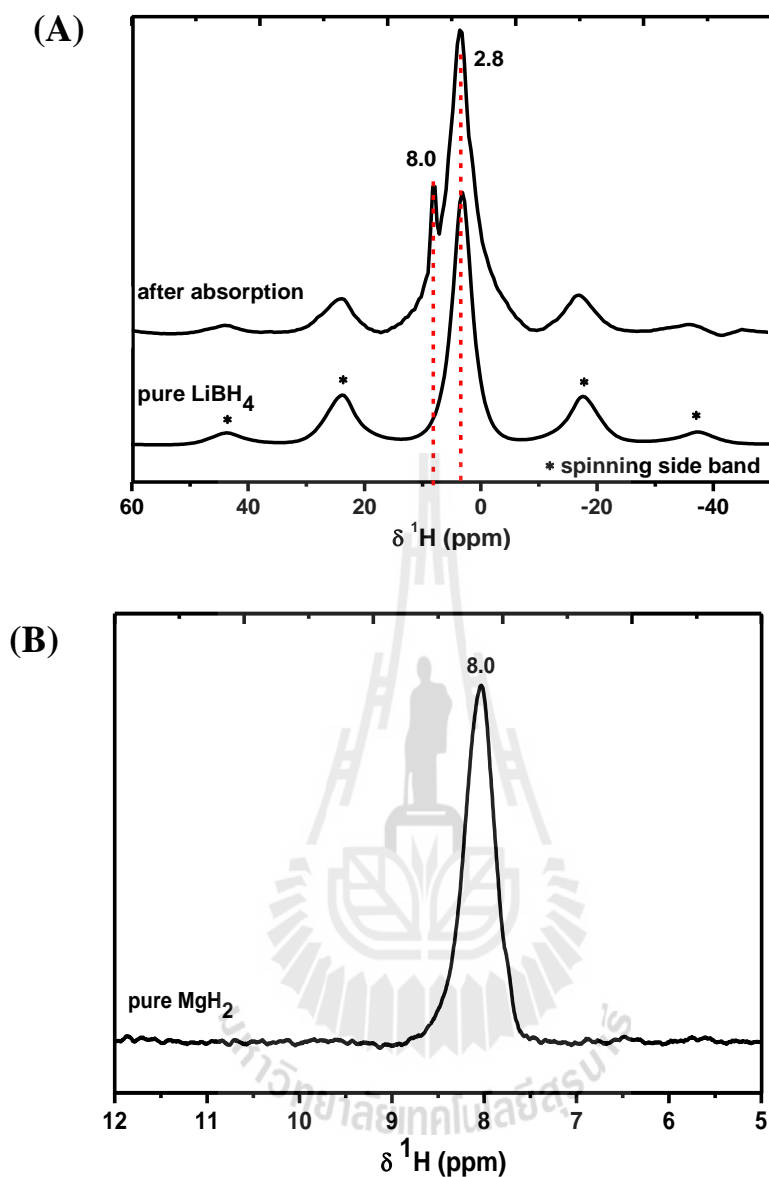


Figure 4.8 ^1H MAS NMR spectra of pure LiBH_4 , nanoconfined 2LiBH_4 -premilled MgH_2 after rehydrogenation (A) and pure MgH_2 (B). The spinning sidebands are marked by a asterisks.

Moreover, the ^{11}B MAS NMR spectra of pure LiBH_4 and nanoconfined LiBH_4 -premilled MgH_2 after rehydrogenation are shown in Figure 4.9. The ^{11}B MAS NMR spectrum of pure LiBH_4 shows the peak at -41.3 ppm (Zhao-Karger *et al.*, 2013). For the sample after rehydrogenation, the ^{11}B MAS NMR peak at -41.3 ppm is also

displayed as, in agreement with LiBH_4 . This indicates that the sample can be successfully reversible and no other borohydride phases (e.g., $\text{Mg}(\text{BH}_4)_2$) occurred during rehydrogenation.

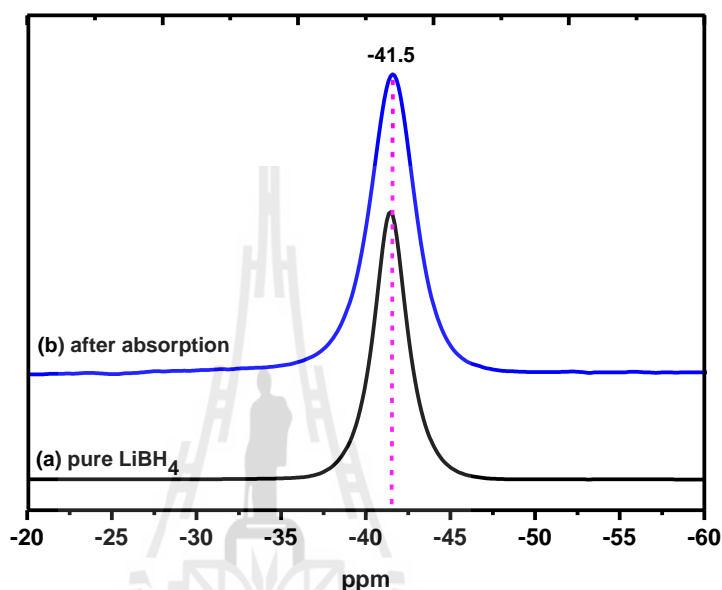


Figure 4.9 ^{11}B MAS NMR spectra of pure LiBH_4 (a) and nanoconfined 2LiBH_4 -premilled MgH_2 after rehydrogenation (b). The spinning sidebands are marked as asterisks.

4.3 Kinetics, reversibility, and hydrogen reproducibility

To study kinetics of the nanoconfined $2\text{LiBH}_4\text{-MgH}_2$ and nanoconfined 2LiBH_4 -premilled MgH_2 , the activation energy of the samples were calculated from DSC technique. The measurement was performed at four different heating rates (β) of 2, 5, 10, and 15 $^\circ\text{C}/\text{min}$. With respect to Kissinger equation (equation 4.2), activation energy (E_A) can be calculated.

$$\ln(\beta/T_p^2) = -E_A/RT + \ln(k_0R/E_A) \quad (4.2)$$

where β is the heating rate, T_p is peak temperature of MgH_2 and $LiBH_4$ during dehydrogenation obtained from DSC results, R is the gas constant ($8.314 \text{ J mol}^{-1} \text{ K}^{-1}$), E_A is the activation energy, and k_0 is the constant (Varin *et al.*, 2009). To calculate the E_A of each heating rates, peak temperatures obtained from curve fitting technique are evaluated (Figure 4.10 (A) for nanoconfined $2LiBH_4$ - MgH_2 and Figure 4.11(A) for nanoconfined $2LiBH_4$ -premilled MgH_2). For Figure 4.10 (A), three endothermic peaks were found for all heating rate. These peaks shift to higher temperature as the heating rate is increased. From the Kissinger plots, the activation energy of each dehydrogenation step is calculated from the slope of the plots as shown in Figure 4.10 (B). The E_A values of 141.8, 262.8, and 135.6 kJ/mol are obtained from the 1st, 2nd, and 3rd dehydrogenation peaks. In the case of nanoconfined $2LiBH_4$ -premilled each DSC thermogram also consists of the dehydrogenation peaks as same as in case of the nanoconfined sample without MgH_2 premilling (Figure 4.11 (A)). From the slope of Kissinger plots (Figure 4.11 (B)), E_A values of 157.8, 124.8, and 184.8 kJ/mol are calculated for the 1st, 2nd, and 3rd dehydrogenation peaks, respectively. From Figures 4.10 (A) and 4.11 (A), the main dehydrogenation of nanoconfined $2LiBH_4$ - MgH_2 belongs to the 1st and 2nd peaks, while that of nanoconfined $2LiBH_4$ -premilled MgH_2 is the 2nd peak. Therefore, dehydrogenation reaction of nanoconfined $2LiBH_4$ - MgH_2 needs 141.6-262.8 kJ/mol for E_A , while that of nanoconfined $2LiBH_4$ -premilled MgH_2 is 124.8 kJ/mol. Therefore, the E_A value of nanoconfined $2LiBH_4$ -premilled MgH_2 is lower than that of nanoconfined $2LiBH_4$ - MgH_2 for about 17.8-138 kJ/mol. This indicates that the dehydrogenation kinetics of nanoconfined $2LiBH_4$ -premilled MgH_2 is faster than that of nanoconfined $2LiBH_4$ - MgH_2 . This relates to the effective

nanoconfinement of MgH_2 and LiBH_4 into CAS as previously discussed in N_2 adsorption-desorption, SEM-EDS-mapping, and simultaneous DSC-TGA-MS results.

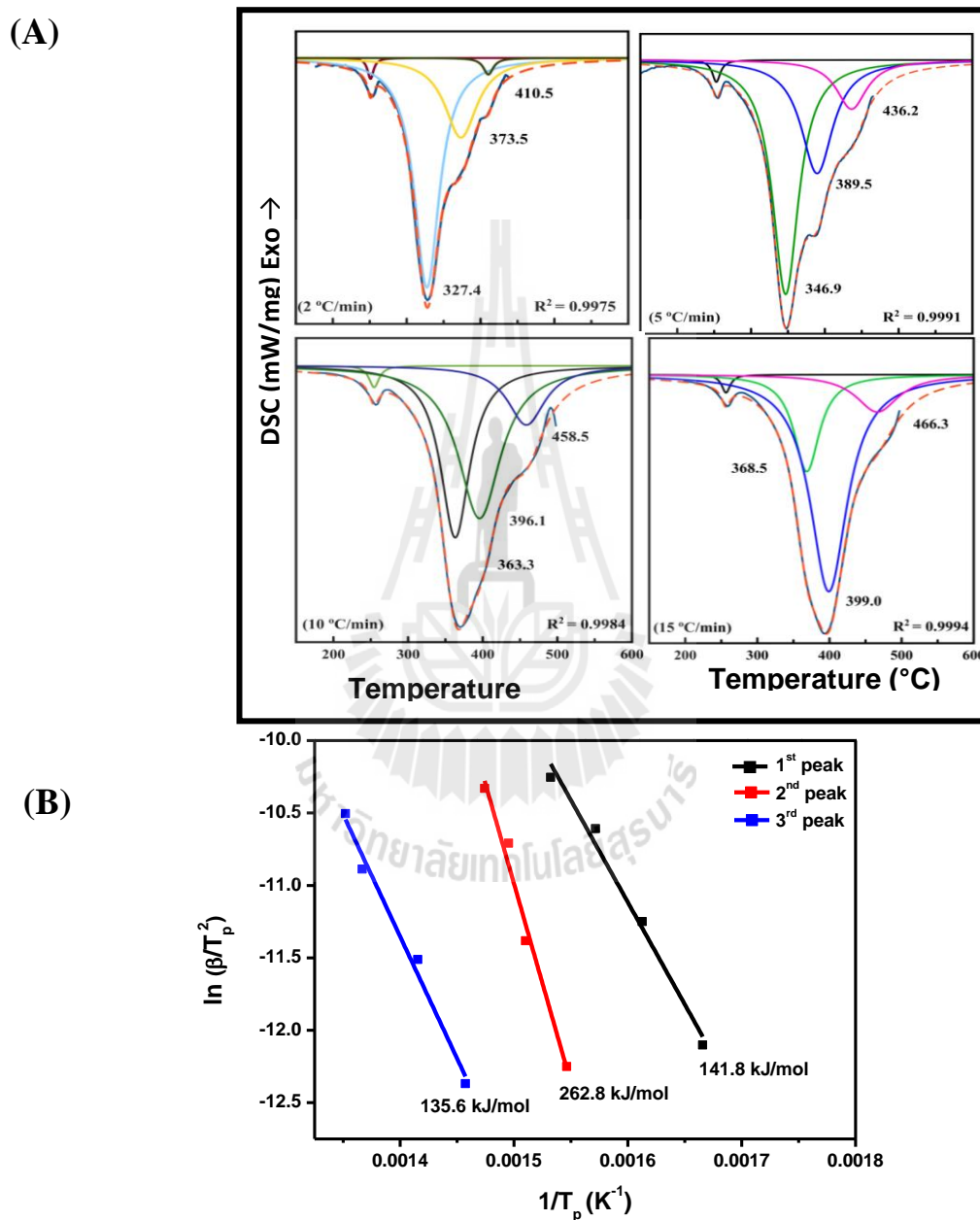


Figure 4.10 DSC curves with deconvolution of several heating rates of nanoconfined $2\text{LiBH}_4\text{-MgH}_2$ (A) and the Kissinger plots representing the activation energy (B).

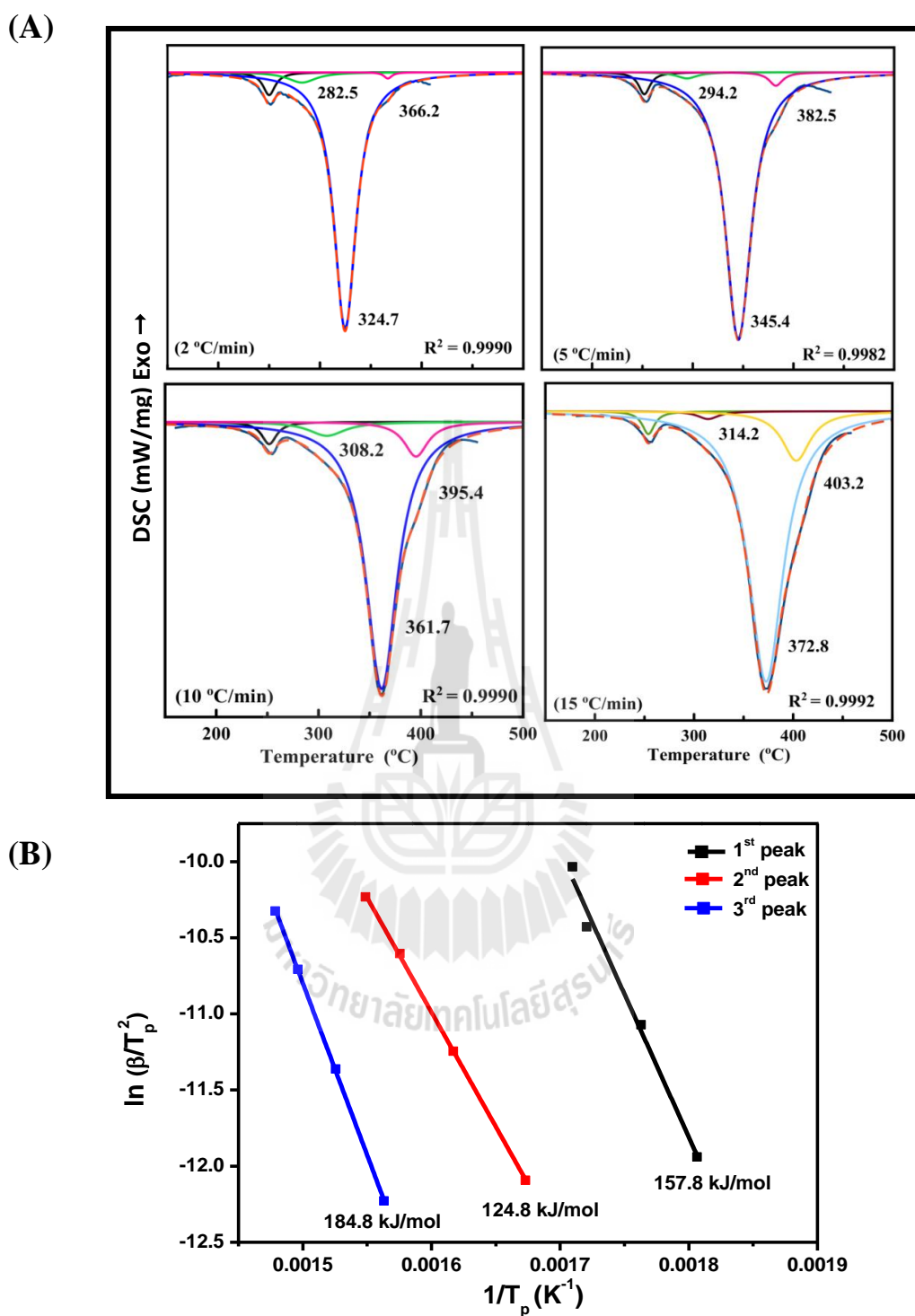


Figure 4.11 DSC curves with deconvolution of several heating rates of nanoconfined 2LiBH_4 -premilled MgH_2 (A) and the Kissinger plots representing the activation energy (B).

To study the reversibility, the dehydrogenation kinetics, and the reproducibility of hydrogen content during cycling of nanoconfined 2LiBH₄-premilled MgH₂, the sample was investigated by using Sievert-type method (Figure 4.12). It is shown as three hydrogen releases and uptake cycles. For the 1st dehydrogenation at 320 °C and $P(\text{H}_2)$ of 3-4 bar H₂, it significantly releases 4.54 wt. % H₂ (9.14 wt. % H₂ is corresponded to the hydride composite content) within 2 h. On the basis of the MS result (Figure 4.4 (B)), where only hydrogen is detected; it can be assured that 4.54 wt. % of gas desorbed from nanoconfined 2LiBH₄-premilled MgH₂ belong to only hydrogen. Lower hydrogen content released during the 1st dehydrogenation of nanoconfined 2LiBH₄-premilled MgH₂ with respect to the theoretical value of 5.7 wt. % H₂ is due to partial dehydrogenation during nanoconfinement confirmed by in situ SR-PXD results, that MgB₂ is formed after melt infiltration (Figure 4.6). Thereafter, the 1st rehydrogenations of nanoconfined 2LiBH₄-premilled MgH₂ was complete at 320-325 °C under 84 bar H₂ for 42 h. It releases hydrogen for 4.96 wt. % (9.95 wt. % H₂ with respect to hydride composite content) in the 2nd dehydrogenation after 12 h. With respect to the 1st dehydrogenation, it is found that the 2nd cycle performs slightly slow kinetics. For the 2nd rehydrogenation, it was carried out under the same pressure and temperature conditions as the 1st cycle for shorter time of 12 h. It releases 4.43 wt. % H₂ (8.88wt. % H₂ with respect to hydride composite content) within 3 h of the 3rd dehydrogenation. From these results (Figure 4.12), it should be noted that the kinetic behavior of the 2nd and 3rd dehydrogenation is comparable as revealed from the overlapping of the kinetic plot. Furthermore, for the inset of the Figure 4.12, two-step dehydrogenations are achieved from the 2nd and 3rd cycles. Moreover, dehydrogenation kinetics of nanoconfined 2LiBH₄-MgH₂ under the same temperature

and pressure condition was also measured for comparison (Figure 4.12). It shows two-step dehydrogenation for 4.30 wt. % gas within 4 h. With respect to DSC-TGA-MS results of nanoconfined $2\text{LiBH}_4\text{-MgH}_2$ (Figure 4.4 (A)), significant amount of B_2H_6 is released together with hydrogen during dehydrogenation. Therefore, 4.30 wt. % of gas from nanoconfined $2\text{LiBH}_4\text{-MgH}_2$ relate to partial hydrogen and B_2H_6 . In addition, the dehydrogenation kinetics of nanoconfined $2\text{LiBH}_4\text{-MgH}_2$ is slower than that of nanoconfined $2\text{LiBH}_4\text{-premilled MgH}_2$.

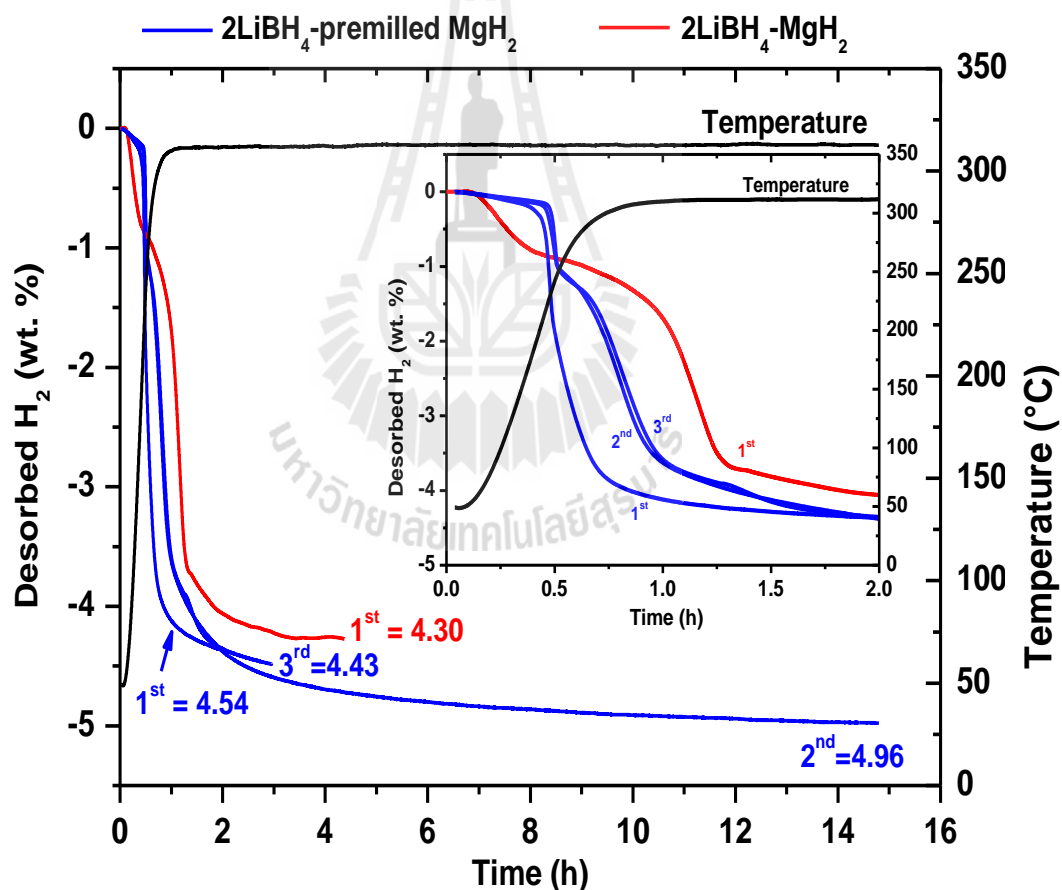


Figure 4.12 The dehydrogenation profile of nanoconfined $2\text{LiBH}_4\text{-MgH}_2$ (red line) and nanoconfined $2\text{LiBH}_4\text{-premilled MgH}_2$ (blue line).

To further assure that there are two steps of reaction for the 2nd and 3rd cycles of nanoconfined 2LiBH₄-premilled MgH₂ the sample after 1st rehydrogenation was evaluated by simultaneous DSC-MS measurements (Figure 4.13). In the DSC result, the phase transformation of LiBH₄ is deficient whereas that of melting disappears. These suggest the enhancement of amorphous LiBH₄ resulted from further nanoconfinement into CAS upon cycling. For the endothermic peak in the temperature range of 255-380 °C, two overlapping steps of dehydrogenation are clarified starting at 255 and 305 °C. In the case of MS result, it shows only hydrogen without B₂H₆ signal.

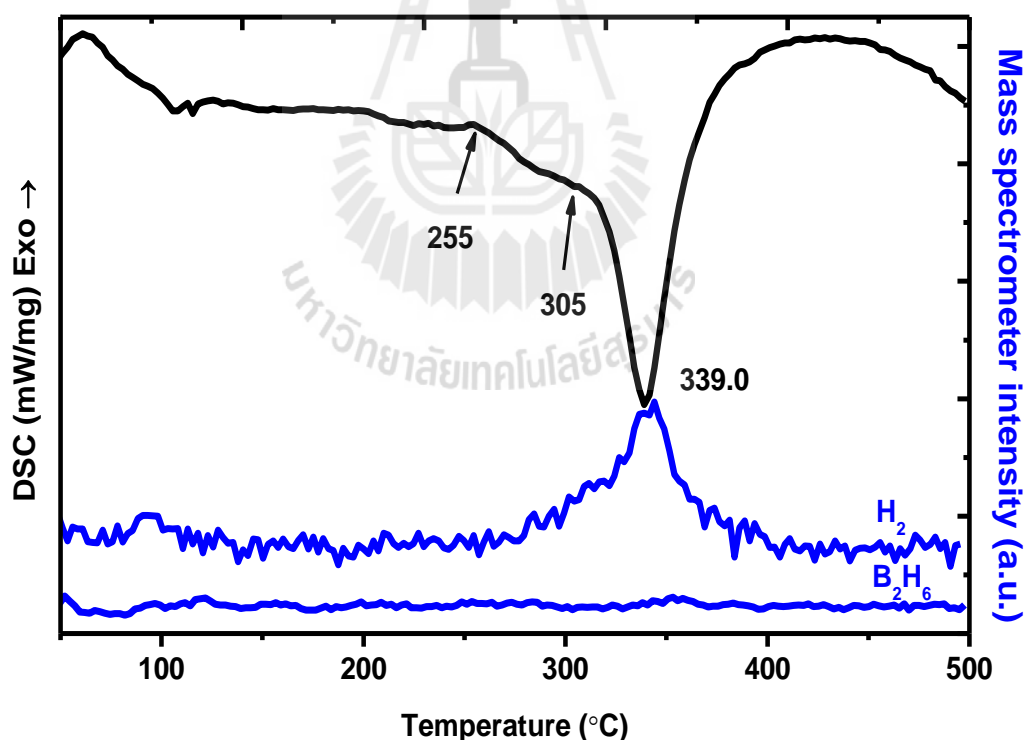


Figure 4.13 Simultaneously performed DSC-MS of the nanoconfined 2LiBH₄-premilled MgH₂ after rehydrogenation.

To evaluate the dehydrogenated phases of nanoconfined 2LiBH_4 -premilled MgH_2 in the 2nd cycle, the powder samples after 1st rehydrogenation and 2nd dehydrogenation at 300 °C for 1 h ($P(\text{H}_2) = 3\text{-}4$ bar H_2) were determined by ^{11}B (Figure 4.14) and ^1H (Figure 4.15) MAS NMR. From Figure 4.14 (a), pure LiBH_4 gives a peak at -41.3 ppm. In the case of the sample after 1st rehydrogenation, a signal peak, referring to LiBH_4 (-41.3 ppm) is observed (Figure 4.14 (b)). For the sample after 2nd dehydrogenation at 300 °C, the ^{11}B MAS NMR signal of LiBH_4 (at -41.3 ppm) is found together with the weak signal at about 1.2 ppm (Figure 4.14 (c)). The latter refers to tetrahedral BO_4 units (Yan *et al.*, 2013). This confirms that there is slight dehydrogenation of LiBH_4 and oxidation in ambient condition during dehydrogenation.

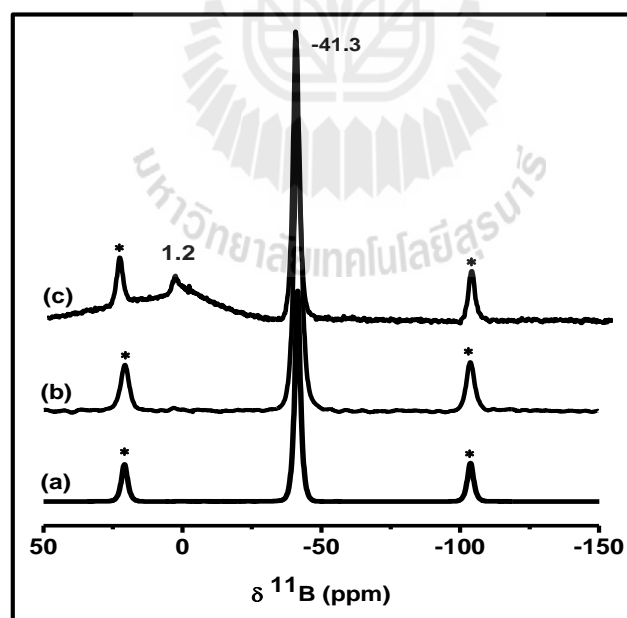


Figure 4.14 ^{11}B MAS NMR spectra of pure LiBH_4 (a), nanoconfined 2LiBH_4 -premilled MgH_2 after rehydrogenation (b), and after 2nd dehydrogenation at 300 °C for 1h (c).

From ^1H MAS NMR, Figures 4.15 (A) and (B) display peaks referring to LiBH_4 and MgH_2 at 2.8 and 8.0 ppm, respectively. After the 1st rehydrogenation, the ^1H MAS NMR signals as LiBH_4 and MgH_2 appear at the same position of LiBH_4 and MgH_2 . This suggests that the sample is completely rehydrogenated. In the case of the sample after 2nd dehydrogenation at 300 °C, signals of both LiBH_4 and MgH_2 are still detected. However, the relative amount of MgH_2 with respect to that of LiBH_4 considerably decreases. From the result, this indicates that the 1st step dehydrogenation at 255-300 °C mainly relates to the dehydrogenation of MgH_2 and slightly corresponds to that of LiBH_4 . For the 2nd step after 300 °C, it can be due to the dehydrogenation of residual MgH_2 and LiBH_4 .

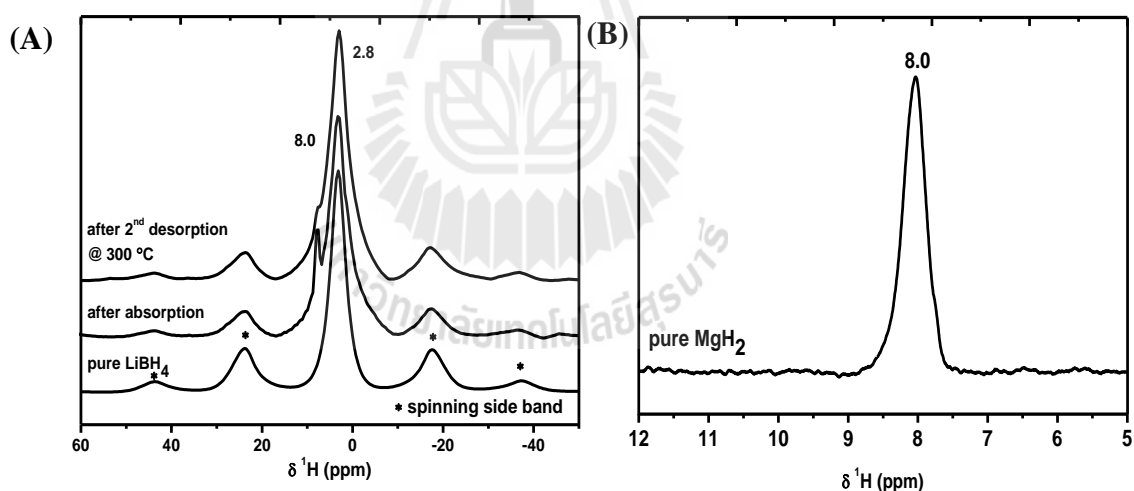


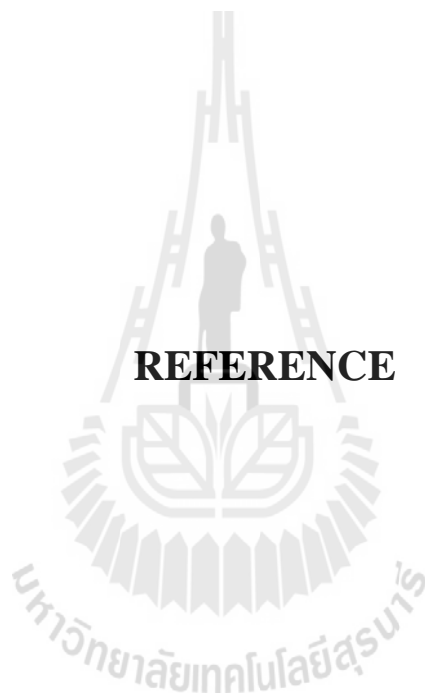
Figure 4.15 ^1H MAS NMR spectra of pure LiBH_4 , nanoconfined 2LiBH_4 -premilled MgH_2 after rehydrogenation, and after 2nd dehydrogenation at 300 °C for 1h (A) and pure MgH_2 (B).

CHAPTER V

CONCLUSION

In this work, nanoconfined $2\text{LiBH}_4\text{-MgH}_2$ and nanoconfined 2LiBH_4 -premilled MgH_2 were successfully prepared by melt infiltration into resorcinol-formaldehyde carbon aerogel scaffold (CAS) for hydrogen storage systems. Nanoconfinement of LiBH_4 and MgH_2 in CAS was confirmed by N_2 adsorption-desorption, SEM-EDS-mapping, and DSC-TGA-MS techniques. Dehydrogenation kinetics, based on activation energy (E_A) was reduced by MgH_2 premilling ($\Delta E_A = 16.8\text{-}138$ kJ/mol). Dehydrogenation of nanoconfined sample without MgH_2 premilling was accomplished at an elevated temperature of 430 °C, together with B_2H_6 release. In the case of the nanoconfined 2LiBH_4 -premilled MgH_2 sample, one-step dehydrogenation was achieved within 400 °C without a B_2H_6 signal. Moreover, the dehydrogenation kinetics of nanoconfined sample with MgH_2 premilling was enhanced as compared with that of the nanoconfined $2\text{LiBH}_4\text{-MgH}_2$. The hydrogen storage capacity was 4.43 wt. %, which desorbed from nanoconfined 2LiBH_4 -premilled MgH_2 in the 1st cycle within 2 h. However, in the 2nd and 3rd dehydrogenation cycles of this sample, two steps of the dehydrogenation were observed. Apparently the first step was mainly the dehydrogenation of MgH_2 and partial that of LiBH_4 . The second step was the dehydrogenation of residual MgH_2 and LiBH_4 .

REFERENCE



REFERENCES

- AEROGEL.ORG. (2014). **Organic and Carbon Aerogels** [On-line]. Available: <http://www.aerogel.org/?p=71>.
- Au, M., and Jurgensen, A. (2006). Modified lithium borohydrides for reversible hydrogen storage. **J. Phys. Chem. B.** 110: 7062-7067.
- Au, M., Jurgensen, A., and Zeigler, K. (2006). Modified lithium borohydrides for reversible hydrogen storage (2). **J. Phys. Chem. B.** 110: 26482-26487.
- Autobloggreen. (2009). First czech hydrogen station to open in the fall [On-line]. Available: <http://green.autoblog.com/2009/05/15/first-czech-hydrogen-station-to-open-in-the-fall/>.
- Bösenberg, U., Doppiu, S., Barkhordarian, G., Eigen, N., Borgschulte, A., and et al. (2007). Hydrogen sorption properties of MgH₂-LiBH₄ composites. **Acta Materialia.** 55: 3951-3958.
- Buhl, J-Ch and Murshed, M. M. (2009). (Na₄BH)³⁺ guests inside aluminosilicate, gallosilicate and aluminogermanate sodalite host frameworks studies by ¹H, ¹¹B, and ²³Na MAS NMR spectroscopy. **Mater. Res. Bull.** 44 :1581-1585.
- Corey, L. R., Shane, T. D., Bowman, C. R., and Conradi, S. M. (2008). Atomic motions in LiBH₄ by NMR. **J. Phys. Chem. C.** 112: 18760-18710.
- Crosby, Kyle. and Shaw, L. L. (2010). Dehydrating and rehydrating properties of high-energy ball milled LiBH₄ + MgH₂ mixtures. *Int. J. Hydrogen Energy* 35: 7519-7529.

- Davidson, M. W. (2014). Hydrogen Fuel Cell Basics [On-line]. Available: <http://micro.magnet.fsu.edu/primer/java/fuelcell/>.
- Dornheim, M. (2005). **Prototype tank for NaAlH₄ based solid state hydrogen storage** [On-line]. Available from: <http://www.flyhy.eu/HZG.html>.
- Freedom CAS&Fuel Partnership. (2009). **Hydrogen Production: Overview of technology options** [On-line]. Available: http://www1.eere.energy.gov/hydrogenandfuelcells/pdfs/h2_tech_roadmap.pdf.
- Future Energies Magazine. (2001-2014). **Fuel Cell Power**. [On-line]. Available: <http://www.futureenergies.com/modules.php?op=modload&name=News&file=article&sid=959>.
- Gosalawit-Utke, R., Milanese, C., Javadian, P., Jepsen, J., Laipple, D., Karimi, F., Puszkiel, J., Jensen, T. R., Marini, A., Klassen, T., and Dornheim, M. (2013). Nanoconfined 2LiBH₄-MgH₂-TiCl₃ in carbonaerogel scaffold for reversible hydrogen storage. **Int. J. Hydrogen Energy** 38:3275-3282.
- Gosalawit-Utke, R., Milanese, C., Nielsen, K. T., Karimi, F., Saldan, I., Pranzas, K., Jensen, T. R., Marini, A., Klassen, T., and Dornheim, M. (2013). Nanoconfined 2LiBH₄-MgH₂ for reversible hydrogen storage: reaction mechanisms, kinetics and thermodynamics. **Int. J. Hydrogen Energy** 38: 1932-1942.
- Gosalawit-Utke, R., Nielsen, T. K., Pranzas, K., Saldan, I., Pistidda, C., Karimi, F., Laipple, D., Skibsted, J., Jensen, T. R., Klassen, T., and Dornheim, M. (2011). 2LiBH₄-MgH₂ in a resorcinol-furfural carbon aerogel scaffold for reversible hydrogen storage. **J. Phys. Chem. C** 116: 1526-1534.
- Gosalawit-Utke, R., Nielsen, T. K., Saldan, I., Laipple, D., Cerenius, Y., Jensen, T. R., Klassen, T., and Dornheim, M. (2011). Nanoconfined 2LiBH₄-MgH₂

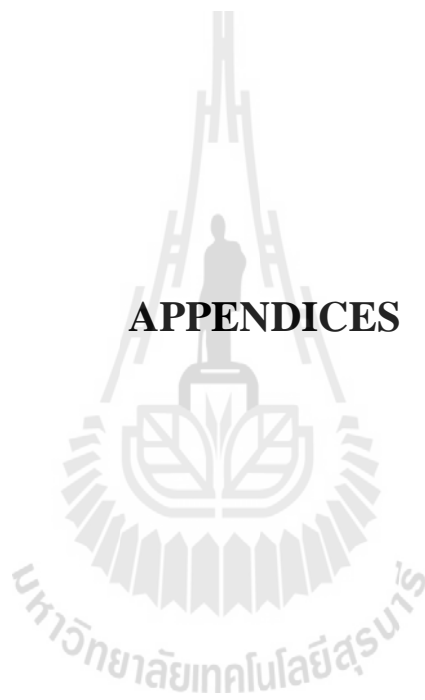
- prepared by direct melt infiltration into nanoporous materials. **J. Phys. Chem. C.** 115: 10903-109010.
- Gross, A. F., Vajo, J. J., Atta, S. L. V., and Olson, G. L. (2008). Enhanced hydrogen storage kinetics of LiBH_4 in nanoporous carbon scaffolds. **J. Phys. Chem. C.** 112: 5651-5657.
- Grzech, A., Lafont, U., Magusin, M. M. C., and Mulder, M. F. (2012) Microscopic study of TiF_3 as hydrogen storage catalyst for MgH_2 . **J. Phys. Chem. C.** 116: 26027-26035.
- Gupta, B. R. (2009). **Hydrogen Fuel: Production, Transport, and Storage.** (pp. 19). USA: CRC Press is an imprint of Taylor & Francis group, LLC.
- Hirscher, M. (2010). **Handbook of Hydrogen Storage: new materials for future energy storage.** (pp. 95). Germany: WILEY-VCH Verlag GmbH & Co. KGaA.
- Léon, A. (2008). **Hydrogen Technology: mobile and portable applications.** (pp. 15-45). Germany: Springer Science in Green Energy and Technology.
- Li, C., Peng, P., Zhou, W. D., and Wan, L. (2011). Research progress in LiBH_4 for hydrogen storage: A review. **Int. J. Hydrogen Energy.** 36: 14512-14526.
- Liu, M. D., Huang, J. W., Si, Z. T., and Zhang, A.Q. (2013). Hydrogen storage properties of LiBH_4 destabilized by SrH_2 . **J. Alloys Compd.** 551: 8-11.
- Liu, X., Peaslee, D., Jost, Z. C., and Majzoub, H. E. (2010). Controlling the Decomposition pathway of LiBH_4 via confinement in highly ordered nanoporous carbon. **J. Phys. Chem. C.** 114: 14036-14041.
- Multidisciplinary project. (2006). **Hydrogen storage materials: metal hydride** [Online]. Available: <http://students.chem.tue.nl/ifp14/Metalhydrides.htm>.

- Nielsen, K. T., Bösenberg, U., Goslawit, R., Dornheim, M., Cerenius, Y., Besenbacher, F., and Jensen, R. T. (2010). A reversible nanoconfinement chemical reaction. **ACS Nano**. 4: 3903-3908.
- Niraj, K. S., Takeshi, K., Oleksandr, D., Jerzy, W. W., Marek, P., and Vitalij, K. P. (2012). Mechanochemical transformations in $\text{NaNH}_2\text{-MgH}_2$ mixtures. **J. Alloy Comp.**153: 324-327.
- Oregonstate.edu. (2008). Other types of hydrogen storage [On-line]. Available: http://www.physics.oregonstate.edu/~demareed/313Wiki/doku.php?id=nanotube_based_hydrogen_storage#introduction.
- Orimo, S., Nakamori, Y., Kitahara, G., Miwa, K., Towata, S., and Zuttler, A. (2005). Dehydrogenating and rehydrogenating reactions of LiBH_4 . **J. Alloys Comp.** 404-406: 427-430.
- Riis, T., Hagen, E. F., Vie, S. J. P., and Ulleberg, Ø. (2006). **Hydrogen Production and Storage** [On-line]. Available: <http://www.iea.org/publications/freepublications/publication/hydrogen.pdf>.
- Ritter, A. J and Al-Muhtaseb, A. S. (2003). Preparation and properties of resorcinol-formaldehyde organic and carbon gels. **Adv. Mater.** 15(2): 101-114.
- Shane, T. D., Corey, L. R., McIntosh, C., Rayhel, H. L., Bowman, C. R., Vajo, J. J., Gross, A. F., and Conradi, M. S. (2010). LiBH_4 in Carbon Aerogel Scaffolds: An NMR Study of Atomic Motions. **J. Phys. Chem. C**. 114: 4008-4014.
- Stolten, D. (2010). **Hydrogen and Fuel Cells**. (pp. 3-14). Germany: WILEY-VCH Verlag GmbH & Co. KGaA.

- Sun, T., Lui, J., Jia, Y., Wang, H., Sun, D., Zhu, M., and Yao, X. (2012). Confined LiBH_4 : enabling fast hydrogen release at $\sim 100^\circ\text{C}$. **Int. J. Hydrogen Energy**. 37: 18920:18926.
- Suryanarayana, C. (2003). Mechanical alloying and milling. **Progress in Materials Science**. 49: 1-184.
- Taube, K. (2010). Solid state hydrogen storage [On-line]. Available: <http://www.flyhy.eu/HZG.html#>.
- Tao, Y., Endo, M., and Kaneko, K. (2008). A Review of Synthesis and Nanopore Structure of Organic Polymer Aerogels and Carbon Aerogel. **Recent Pat. Chem Eng**. 1: 192-200.
- Vajo, J. J., Salguero, T. T., Gross, A. F., Skeith L, S., and Olson, L. G. (2007). Thermodynamic destabilization and reaction kinetics in light metal hydride systems. **J. Alloys. Comp.** 446-447: 409-414.
- Vajo, J. J., Skeith, L. S., and Mertens, F. (2005). Reversible storage of hydrogen in destabilized LiBH_4 . **J. Phys. Chem. B**. 109: 3719-3722.
- Varin R, A., Czujko, T., and Wronski, Z. S. (2009). **Nanomaterials for solid state hydrogen storage**. (pp 3-4). USA: Springer Science and Business Media.
- Wikipedia. (2013). **Activation energy** [On-line]. Available: http://commons.wikimedia.org/wiki/File:Activation_energy.svg.
- Xu, J., Meng, R., Cao, J., Gu, X., Qi, Z., Wang, W., and Chen, Z. (2013). Enhanced dehydrogenation and rehydrogenation properties of LiBH_4 catalyzed by grapheme. **Int. J. Hydrogen Energy**. 38:2796-2803.

- Xu, J., Wang, A., and Zhang, T. (2012). A two-step synthesis of ordered mesoporous resorcinol-formaldehyde polymer and carbon. **Carbon**. 50:1807-1816.
- Yan, Y., Remhof, A., Mauron, P., Rentsch, D., Lodzianna, Z., Lee, Y-S., Lee, H-S., Cho, Y. W., and Züttle, A. (2013). Controlling the Dehydrogenation Reaction toward Reversibility of the $\text{LiBH}_4\text{-Ca}(\text{BH}_4)_2$ Eutectic System. **J. Phys. Chem. C**. 117: 8878-86.
- Zhang, S., Gross, A. F., Atta, V. L. S., Lopez, M., Liu, P., Ahn, C. C., Vajo, J. J., and Jensen, C. M. (2009). The synthesis and hydrogen storage properties of a MgH_2 incorporated carbon aerogel scaffold. **Nanotechnology**. 20: 204027-204033.
- Zhang, Y., Zhang, W-S., Wang, A-Q., Sun, L-X., Fan, M-Q., Chu, H-L., Sun, J-C., and Zhang, T. (2007). LiBH_4 nanoparticles supported by disordered mesoporous carbon: Hydrogen storage performances and destabilization mechanisms. **Int. J. Hydrogen Energy**. 32: 3976-3980.
- Zhao-K, Z., Witter, R., Bardaji, G. E., Wang, D., Cossement, D., and Fichtner, M. (2013). Altered reaction pathway of eutectic $\text{LiBH}_4\text{-Mg}(\text{BH}_4)_2$ by nanoconfinement. **J. Mater. Chem. A**. 1: 3379-3389.
- Züttle, A., Borgschulte, A., and Schlapbach, L. (2008). **Hydrogen as a Future Energy Carrier**. (pp. 1-6). Germany: WILEY-VCH Verg GmbH & Co. KGaA.
- Züttel, A., Wenger, P., Rentsch, S., Sudan, P., Mauron, Ph., and Emmenegger, Ch. (2003). LiBH_4 a new hydrogen storage material. **J. Power Sources**. 118: 1-7.

APPENDICES



APPENDIX A
CALCULATON FOR SYNTHESIS OF CARBON
AEROGEL SCAFFOLD AND HYDROGEN STORAGE
CAPACITY

มหาวิทยาลัยเทคโนโลยีสุรนารี

A1. Calculation for synthesis of CAS

Resorcinol: Formaldehyde: Na₂CO₃: H₂O = 1: 2: 0.005: 10 in molar ratio

Resorcinol (Mw = 110.01 g/mol) 20.7000 g

$$\begin{aligned} M &= 20.7000 \text{ g} / 110.01 \text{ g/mol} \\ &= 0.188 \text{ mol} \end{aligned}$$

Resorcinol: 2Formaldehyde (Mw = 30.03 g/mol)

$$\begin{aligned} &= 2 \times 0.188 \text{ mol} \\ &= 0.376 \text{ mol} \\ &= 0.376 \text{ mol} \times 30.03 \text{ g/mol} \\ &= 11.29 \text{ g} \end{aligned}$$

Resorcinol: 0.005Na₂CO₃ (Mw=106 g/mol)

$$\begin{aligned} &= 0.005 \times 0.188 \text{ mol} \\ &= 0.00094 \text{ mol} \\ &= 0.00094 \times 106.00 \text{ g/mol} \\ &= 0.0996 \text{ g} \end{aligned}$$

Resorcinol:10H₂O (Mw = 18 .00 g/mol)

$$\begin{aligned} &= 10 \times 0.188 \text{ mol} \\ &= 1.88 \text{ mol} \\ &= 1.88 \text{ mol} \times 18.00 \text{ g/mol} \\ &= 33.84 \text{ g} \end{aligned}$$

Resorcinol = 20.7000 g

Formaldehyde = 11.29 g

Na₂CO₃ = 0.0996 g

$$\text{H}_2\text{O} = 33.84 \text{ g}$$

A2. Calculation molar ratio of 2LiBH₄-MgH₂ mixture

2LiBH₄:MgH₂

$$2\text{LiBH}_4 \text{ Mw} = 21.80 \text{ g/mol}, \quad \text{MgH}_2 \text{ Mw} = 26.30 \text{ g/mol}$$

$$\text{MgH}_2 = \frac{1.0047 \text{ g}}{26.30 \text{ g/mol}}$$

$$= 0.038 \text{ mol}$$

$$2\text{LiBH}_4 = 0.038 \text{ mol} \times (2 \times 21.8 \text{ g/mol})$$

$$= 1.65 \text{ g}$$

$$\text{➤ MgH}_2 = 1.0047 \text{ g}, \quad 2\text{LiBH}_4 = 1.65 \text{ g}$$

A3. Calculation of theoretical hydrogen storage capacity

CAS:2LiBH₄-MgH₂ (1:1 weight ratio)

$$\text{CAS} = 0.5023 \text{ g}, \quad 2\text{LiBH}_4\text{-MgH}_2 = 0.5043 \text{ g}$$

$$\text{wt. \% of } 2\text{LiBH}_4\text{-MgH}_2 = 11.4 \text{ wt. \%}$$

From 11.4 wt. % of hydrogen released by 2LiBH₄-MgH₂, the theoretical hydrogen storage capacity of nanoconfined 2LiBH₄-MgH₂ is calculated by:

$$= 11.4 \text{ wt. \% H}_2$$

$$= 5.7 \text{ wt. \% H}_2$$

A4. The calculation of hydrogen desorption capacity (for example)

➤ For 1st dehydrogenation of the nanoconfined 2LiBH₄-MgH₂

$$T = 320 \text{ }^\circ\text{C} + 273 = 593 \text{ K}$$

$$P1 = 3.2 \text{ atm}$$

$$P2 = 5.5 \text{ atm}$$

$$V = 0.02285 \text{ L}$$

$$R = 0.0821 \text{ L atm K}^{-1} \text{ mol}^{-1}$$

$$g \text{ (sample weight)} = 0.0510 \text{ g}$$

$$(\Delta P)V = nRT$$

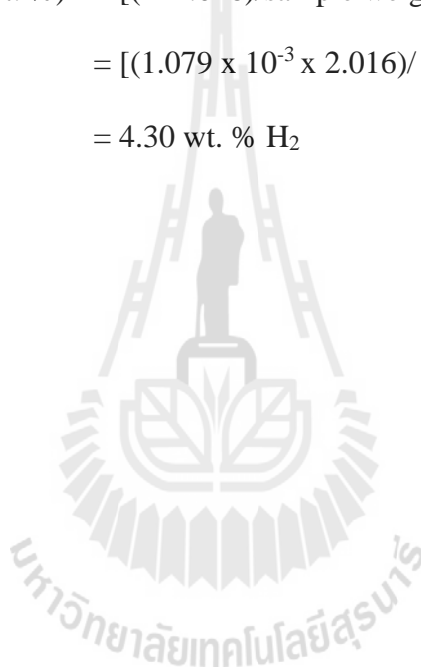
$$n = [2.3 \text{ atm} \times 0.02285 \text{ L}] / [0.0821 \text{ L atm K}^{-1} \text{ mol}^{-1} \times 593 \text{ K}]$$

$$= 1.079 \times 10^{-3} \text{ mol}$$

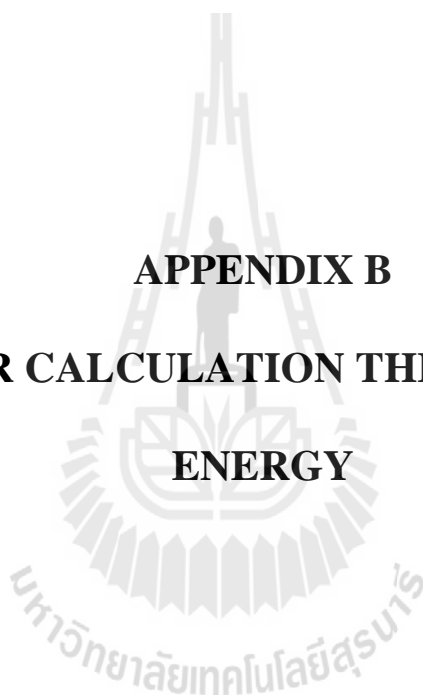
$$\text{H}_2 \text{ desorbed (wt. \%)} = [(n \times 2.016) / \text{sample weight}] \times 100$$

$$= [(1.079 \times 10^{-3} \times 2.016) / 0.0510 \text{ g}] \times 100$$

$$= 4.30 \text{ wt. \% H}_2$$

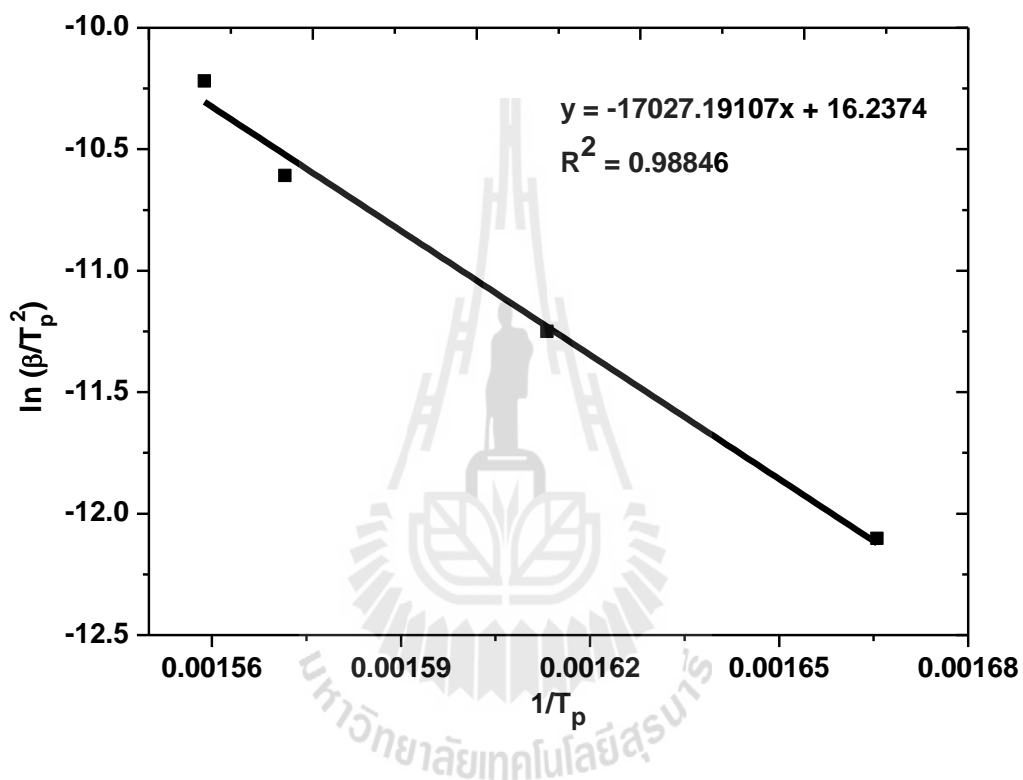


APPENDIX B
DATA FOR CALCULATION THE ACTIVATION
ENERGY



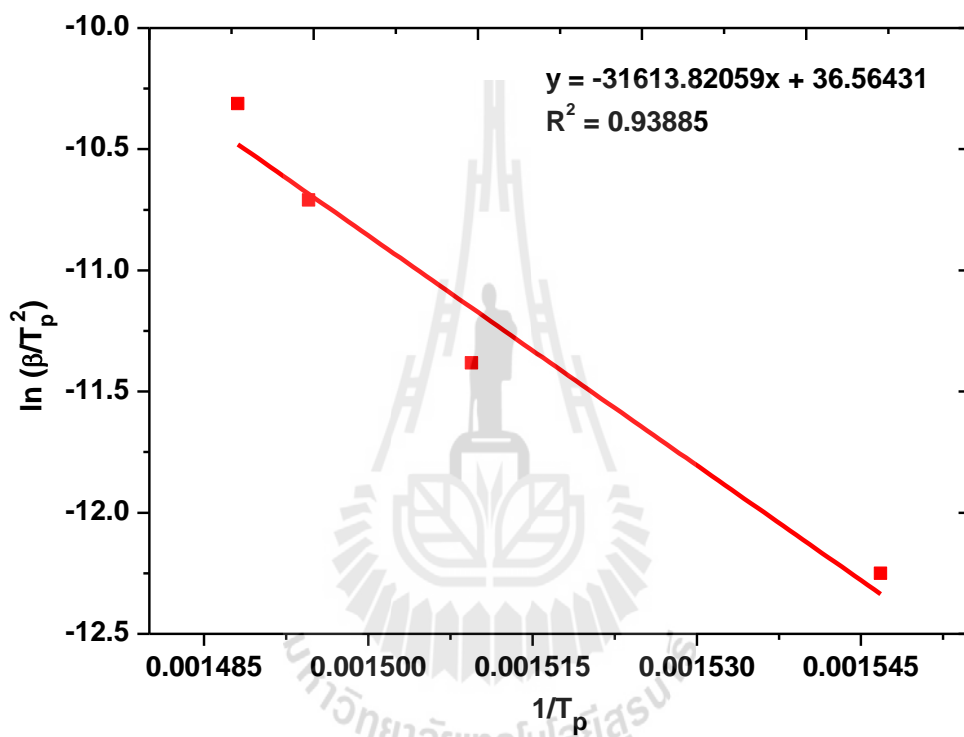
Nanoconfined 2LiBH₄-MgH₂ (1st peak)

β (oC/min)	T _p (oC)	T _p (K)	β/T_p^2	$\ln(\beta/T_p^2)$	1/T _p (K)
2	327.4	600.4	5.55×10^{-06}	-12.102045	0.001666
5	346.9	619.9	1.30×10^{-05}	-11.249678	0.001613
10	363.3	636.3	2.47×10^{-05}	-10.608755	0.001572
15	368.5	641.5	3.65×10^{-05}	-10.219568	0.001559



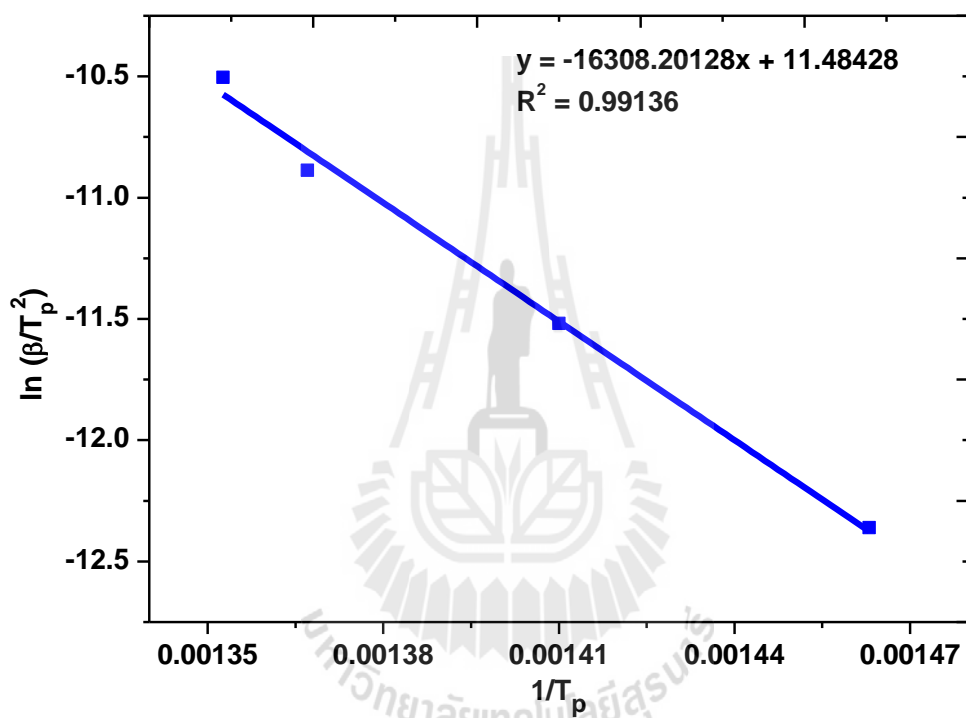
Nanoconfined 2LiBH₄-MgH₂ (2nd peak)

β (oC/min)	T _p (oC)	T _p (K)	β/T_p^2	ln (β/T_p^2)	1/T _p (K)
2	373.5	646.5	4.79x10 ⁻⁰⁶	-12.249999	0.001547
5	389.5	662.5	1.14x10 ⁻⁰⁵	-11.382603	0.001509
10	396.1	669.1	2.23x10 ⁻⁰⁵	-10.709282	0.001495
15	399.0	672.0	3.32x10 ⁻⁰⁵	-10.312466	0.001488



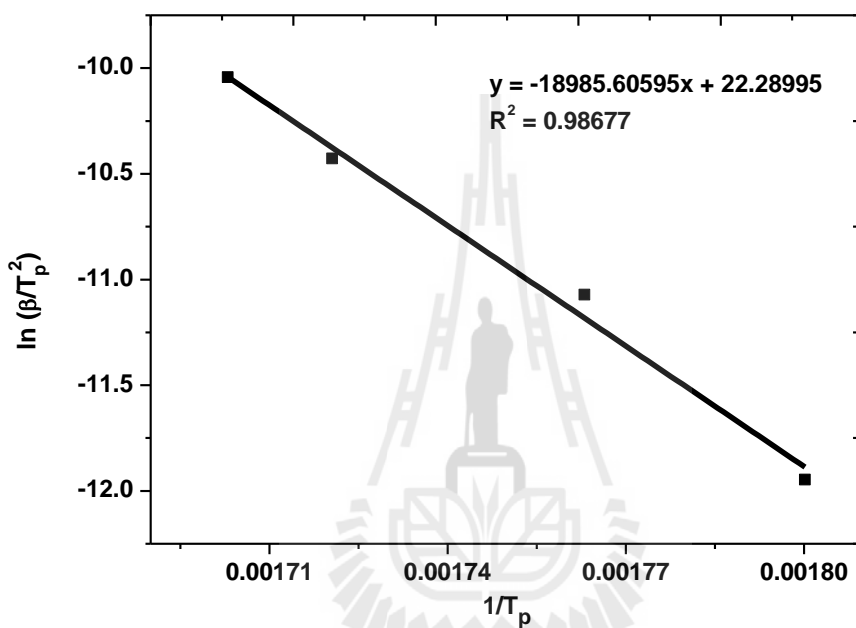
Nanoconfined 2LiBH₄-MgH₂ (3rd peak)

β (oC/min)	T _p (oC)	T _p (K)	β/T_p^2	ln (β/T_p^2)	1/T _p (K)
2	410.5	683.5	4.28E-06	-12.361306	0.001463
5	436.2	709.2	9.94E-06	-11.518837	0.00141
10	458.5	731.5	1.87E-05	-10.887609	0.001367
15	466.3	739.3	2.74E-05	-10.503357	0.001353



Nanoconfined 2LiBH₄-premilled MgH₂ (1st peak)

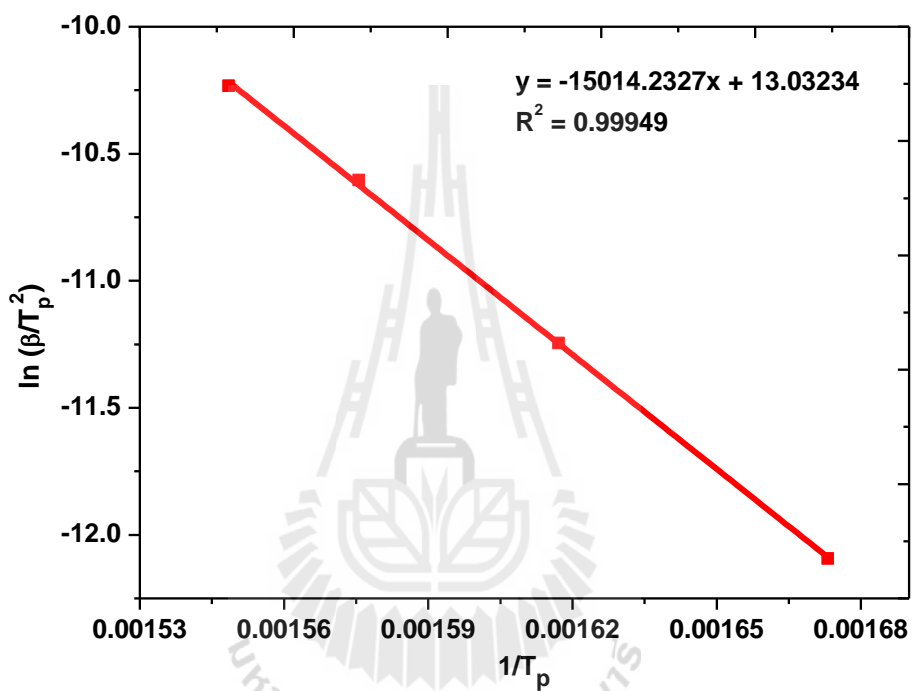
β (°C/min)	T_p (°C)	T_p (K)	β/T_p^2	$\ln(\beta/T_p^2)$	$1/T_p$ (K)
2	282.5	555.5	6.5E-06	-11.9466	0.0018002
5	294.2	567.2	1.6E-05	-11.072	0.0017630
10	308.2	581.2	3E-05	-10.4276	0.0017206
15	314.2	587.2	4.4E-05	-10.0427	0.0017030



มหาวิทยาลัยเทคโนโลยีสุรนารี

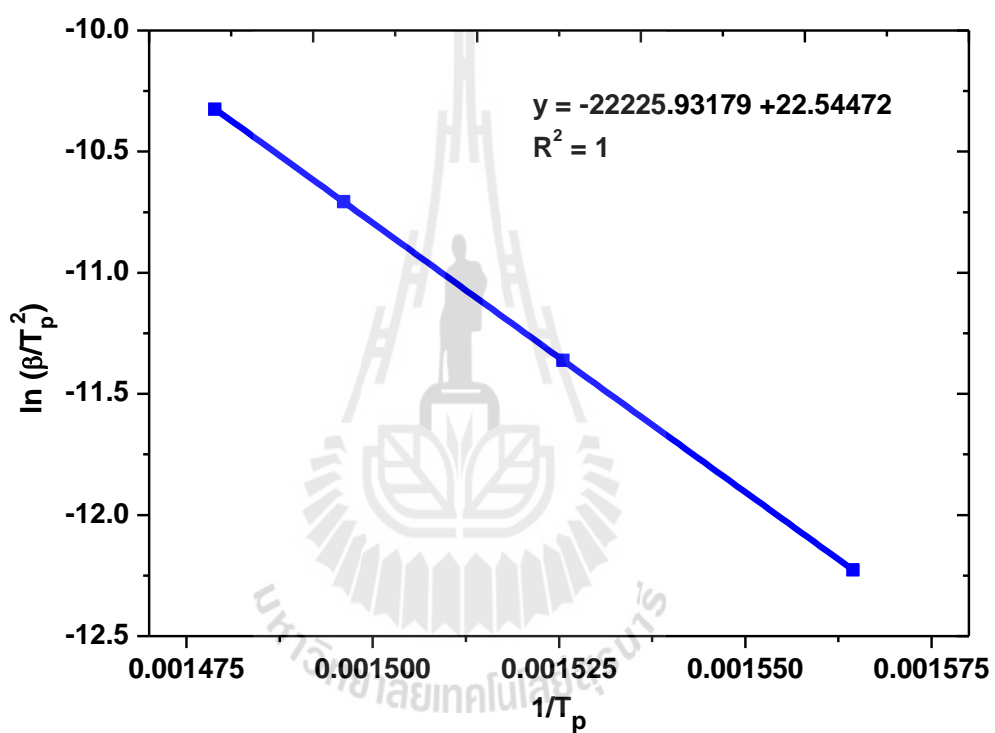
Nanoconfined 2LiBH₄-premilled MgH₂ (2nd peak)

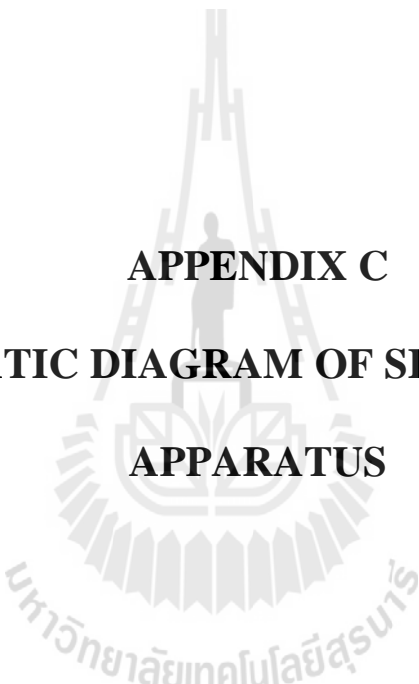
β (°C/min)	T_p (°C)	T_p (K)	β/T_p^2	$\ln(\beta/T_p^2)$	$1/T_p$ (K)
2	324.7	597.7	5.6E-06	-12.093	0.0016731
5	345.4	618.4	1.3E-05	-11.2448	0.0016171
10	361.7	634.7	2.5E-05	-10.6037	0.0015755
15	372.8	645.8	3.6E-05	-10.2329	0.0015485



Nanoconfined 2LiBH₄-premilled MgH₂ (3rd peak)

β (°C/min)	T_p (°C)	T_p (K)	β/T_p^2	$\ln(\beta/T_p^2)$	$1/T_p$ (K)
2	366.2	639.2	4.9E-06	-12.2273	0.0015645
5	382.5	655.5	1.2E-05	-11.3614	0.0015256
10	395.4	668.4	2.2E-05	-10.7072	0.0014961
15	403.2	676.2	3.3E-05	-10.3249	0.0014789

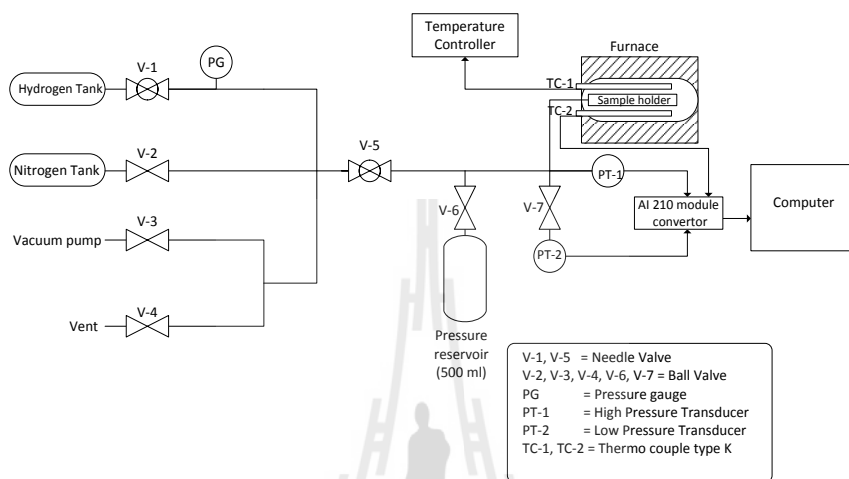




APPENDIX C
SCHEMATIC DIAGRAM OF SIEVERT-TYPE
APPARATUS

มหาวิทยาลัยเทคโนโลยีสุรนารี

C1. Schematic diagrams showing the working principles of the Sievert-type apparatus assembled in the Chemistry Laboratory (F2).



มหาวิทยาลัยเทคโนโลยีสุรนารี

CURRICULUM VITAE

Name Miss Sophida Tiangwiriya

Born July 1st, 1988 in Nakhon Ratchasima, Thailand

Citizenship Thai

Address 11 Moo 9, Tambon Prasuk, Amphor Chumchaung, Nakhon Ratchasima, 30270, Thailand

E-mail sophida007@hotmail.com

Education

2007-2010 B.Sc. (Chemistry), Rajamankala University of Technology Isan Thailand

2011-present M.Sc. (Chemistry), Suranaree University of Technology, Thailand

Presentation and publication:

Sophida Tiangwiriya, Rapee Gosalawit-Utke, Claudio Pistidda, Chiara Milanese, Daniel Laipple, Amedeo Marni, Thomas Klassen, Martin Dornheim, Payam Javadian, Torben R. Jensen. Nanoconfinement of Pre-milled MgH₂-LiBH₄ in Carbon Aerogel Scaffold for Reversible Hydrogen Storage. Presented at the Pure and Applied Chemistry International Conference (PACCON), Khon Kaen, Thailand, 2014 (best oral presentation).